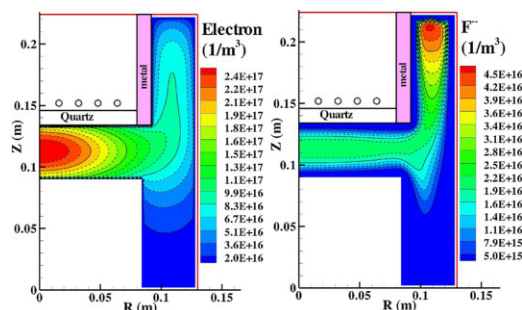


Parallel 2D Axisymmetric Fluid Modeling of CF_4 Discharge in an Inductively Coupled Plasma Source During SiO_2 Etching

Yuan-Ming Chiu, Chung-Hua Chiang, Chieh-Tsan Hung, Meng-Hua Hu, Jong-Shinn Wu,* Feng-Nan Hwang

A parallel 2D axisymmetric plasma fluid modeling for an inductively coupled plasma source with tetrafluoromethane precursor is reported. In total, 32 species with 96 gas-phase and 27 surface reactions with site-balance equations are considered. The predicted results of major species densities are in reasonable agreement with reported experiments. The etching products, e.g. SiF_x and O_2 , are found to be appreciable ($\sim 10\%$) compared to the precursor near the substrate. The predicted density trends, such as CF_x^+ and CF_x ($x = 1-3$), are also consistent with reported experiments. Finally, the predicted etching rate on the SiO_2 substrate is presented and discussed in detail.



1. Introduction

Plasma processing plays an important role in many semiconductor related material fabrication processes, such as surface modification and cleaning,^[1] deposition of thin film for oxide layer,^[2,3] atomic layer deposition,^[4,5] and functional layer such as solar cells^[6] and silicon etching with high-aspect ratios,^[7] among others. In particular, inductively coupled plasma sources (ICPs) have been important processing tools for semiconductor etching and nano-material deposition because of its several advantages, such as operation at low pressure, high plasma density, controllable energetic ions, and generation of

abundant chemically active radical species.^[8] Especially, tetrafluoromethane (CF_4) ICPs have been used very often in plasma etching of dielectric layer. Such etching process usually damages and charges Si or SiO_2 contact layer. Hence, selectivity of SiO_2 and etching rates are extremely important during an etching process.^[9,10] Though the development of plasma etching reactors and processes that is strongly based on trial-and-error method has been shown to be satisfactory for industrial purpose, it may become difficult and less efficient as more complicated chamber design and process is required. Besides, measurements of plasma properties in an ICP chamber are generally difficult and expensive, while plasma modeling could be an invaluable tool for understanding the details of related complex plasma physics and chemistry. Thus, an accurate plasma modeling can contribute greatly to the development of plasma reactors or sources with enhanced performance at a much lower cost.

The methods employed for simulation and modeling of low-temperature plasma processes include the global model, the fluid model, the particle-in-cell with Monte-Carlo collision (PIC-MCC) and the hybrid PIC-fluid model. Among these models, the fluid model is frequently used to study the major plasma physics and chemistry of

Dr. Y.-M. Chiu, Dr. C.-T. Hung, Dr. M.-H. Hu, Prof. J.-S. Wu
Department of Mechanical Engineering, National Chiao Tung
University, Hsinchu 30010, Taiwan
E-mail: chongsin@faculty.nctu.edu.tw

Prof. C.-H. Chiang
Department of Mechanical and Automation Engineering, I-Shou
University, Kaohsiung City 84001, Taiwan

Prof. F.-N. Hwang
Department of Mathematics, National Central University, Zhongli
32001, Taiwan

high-density and low-pressure ICPs under the assumption of sufficient collisions.^[11–13] The models for studying tetrafluoromethane (CF₄) plasma in either capacitive coupled plasma or inductively coupled plasma used for etching purpose have been reported. These include the global models with complex gas-phase reactions^[14–17] and the fluid models considering feeding gas-phase reactions and highly simplified surface reactions using the concept of stick coefficients without taking any etching products into account.^[18–21] However, the consideration of etching products from the substrate is critical in faithfully modeling of these discharges since they can significantly influence the composition of the gas phase species in CF₄ discharge for the etching of SiO₂ and Si.^[22] Several experimental studies that demonstrate its importance are described next in turn.

The etching of SiO₂, which consumes F atom forms SiF₄, and the oxygen releases during etching process. In addition, CF_x radicals react with SiO₂ and form CO, CO₂, and COF₂. These etching products were observed as important gas-phase reactants by several experiments. Coburn et al.^[23] found that the escaping oxygen hinders polymerization on the SiO₂ surface through forming volatile CO, CO₂, and COF₂, which allows etching process to continue without feeding oxygen. The etching products from the quartz such as COF_x⁺, CO⁺, and oxygen radical were detected by a mass spectrometer in CF₄ and CF₄/Ar ICPs.^[24,25] Hebner^[26,27] observed the spatially non-uniform concentrations of etching products SiF and SiF₂ by means of a laser-induced fluorescence in the inductively driven C₂F₆ and C₄F₈ discharges. Cruden et al.^[28,29] examined the etching products SiF₄, CO and COF₂ in CF₄ plasma using the Fourier transform infrared spectroscopy (FTIR). Significant amounts of etch products, such as SiF_x⁺/COF_x⁺ ($x = 1–3$), of quartz window were also detected by Rao et al.^[30,31] and Zhou et al.^[32] Hikosaka et al.^[33] used a quadrupole mass spectrometer (QMS) to measure gas composition in a high-power CF₄ discharge. CO and SiF₃ were found due to the etching of quartz (SiO₂) window, which significantly deteriorated the etching selectivity of SiO₂ in an ICP reactor. To summarize, for an accurate modeling of CF₄ ICP discharge and the surface etching profile, fluid model has to consider not only the gas-phase plasma chemistry but also the surface reactions.

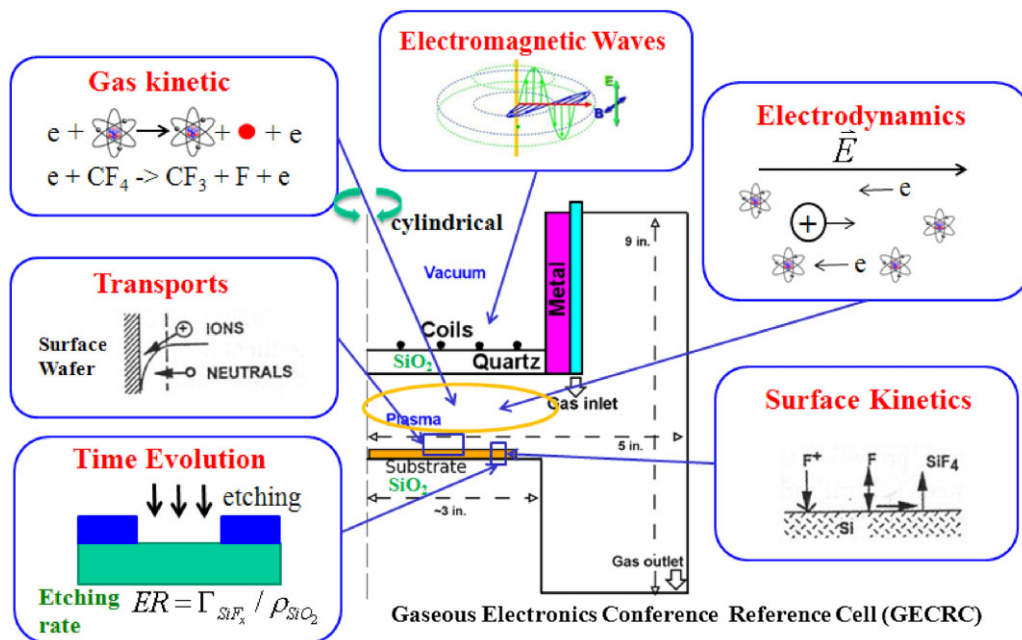
Because the etching products are important as well as the gas-phase reactants resulting from the feedstock gases in a high-density plasma, both the complex gas and surface chemical reactions in CF₄ plasma have to be considered simultaneously in fluid model to reproduce the major characteristics of etching process. Zhang and Kushner^[34] were the pioneers working on combination of plasma gas and surface model, in which they self-consistently coupled a hybrid model and a surface kinetics model to simulate the etching process of Si in a CF₄ discharge. Fukumoto et al.^[35] employed a fluid model coupling with a surface site balance

model to simulate the CF₄ plasma etching of SiO₂ in a reactor with simple geometry without considering detailed gas-phase reactions of CF₄. The power deposition of the inductive electric field is obtained by solving the azimuthal Maxwell's equations in the frequency domain, where the field induced by the coil current is described by the Biot-Savart's law. In addition, the computational time may become prohibitively high for the fluid modeling when considering very complex gas phase and surface reactions. Thus, how to speed up the fluid modeling for a realistic CF₄ ICP is important.

In this study, a parallel 2D axisymmetric fluid model for general inductively coupled plasmas considering the surface site balance model is developed and implemented using the domain decomposition method on the distributed-memory machines through MPI (message passing interface). The developed code is applied to study the complex plasma physics and chemistry of an ICP with CF₄ gas as the feedstock. The azimuthal electric field was solved by the Maxwell's equations through phasor representation and electrostatic field is obtained by the flux balance of charged species under the assumption of ambipolar diffusion. In the current fluid model, in addition to more advanced numerical schemes and parallel computing, much more thorough chemical kinetics, including 32 species, 96 gas reactions and 27 surface reactions are considered to predict the etching rate and etching profile on the substrate, in which the surface site balance model is implemented to describe the etching products from the SiO₂ substrate and quartz windows. The parallel performance and detailed simulation results of plasma physics and chemistry in the gaseous electronics conference reference cell (GECRC) are presented and discussed. Finally, the major findings of the present study are summarized at the end of the paper.

2. Numerical Methods

Figure 1 shows schematically the major physical and chemical processes in an ICP within a GECRC that we would like to model in the simulation. Because Knudsen number ($Kn = \lambda/L$, where λ is mean free path and L is the characteristic length of the reactor) is approximately 0.05 for the electron and 0.01 for the CF₄, the fluid (or continuum) approximation is still considered to be approximately valid, although it may fall into the slip region. Indeed, one has to apply the particle method for modeling the discharge with even lower pressure as compared to the current study. For the feedstock CF₄, the Peclet number ($Pe = LU/D$, where U is the characteristic velocity and D is the mass diffusion coefficient) is approximately 0.09, and the Reynolds number at the inlet ($Re = LU\rho/\mu$, where ρ is the mass density and μ is the viscosity) is approximately 1,200. The



■ Figure 1. The schematic diagram of the dominant processes in a CF_4 discharge reactor for etching SiO_2 .

above shows that it is a diffusion-dominated gas flow. Thus, we only consider diffusion transport for neutral species in the simulation. To sum up, the modeling equations, which we consider include the continuity equations for ions, the momentum equations for ions with the drift-diffusion approximation, the continuity equations for neutral species, the electron energy density equation, and the Maxwell's equation. The electron number density and the static electric field are obtained through the ambipolar diffusion approximation. They are described in the following in turn.

3. Transport Equations for Charged Species

The continuity equation for ions is generally written as

$$\frac{\partial n_i}{\partial t} + \nabla \cdot \vec{\Gamma}_i = R_{i,source} - R_{i,sink} \quad (1)$$

where n_i is the i th ion number density, $R_{i,source}$ and $R_{i,sink}$ are source and sink terms of i th ion species, respectively, resulting from chemical reactions. Based on the drift-diffusion approximation, $\vec{\Gamma}_i$ is the i th ion flux that can be written as

$$\vec{\Gamma}_i = -D_i \nabla n_i \pm \mu_i n_i \vec{E} \quad (2)$$

where \vec{E} , μ_i , and D_i are the electrostatic field, the mobility of i th ion, and the diffusivity of i th ion, respectively. In the current study, the mobility of the i th ion in background

neutral species j is calculated by using the Langevin mobility expression at low electric field and the mobility of the i th ion in the background gas mixture is obtained using the Blancs law.^[36] In addition, the corresponding diffusivities of all ion species are calculated through the Einstein relation. The Neumann boundary conditions for all ions are applied at the asymmetric axis. The boundary condition at wall for all positive ions is set to be a Bohm flux type as $\Gamma_i = 0.61 n_i \sqrt{8kT_e/M_i}$, while the negative ion fluxes at wall are all equal to zero since they rebound back by the sheath.

Since the sheath thickness is typically less than mm in a high-density electronegative plasma, we do not resolve sheath dynamics near the boundaries of reactor walls in the simulation. The ambipolar diffusion approximation of the ions and electron are assumed,^[35,37,38] which the electrostatic field can be written as

$$\vec{E}_{r,z} = \frac{\sum_+ D_+ n_+ - \sum_- D_- n_-}{\sum_+ \mu_+ n_+ + \sum_- \mu_- n_-} \quad (3)$$

The total fluxes of the charged species satisfy the following relation,

$$\sum_+ \Gamma_+ = \sum_- \Gamma_- \quad (4)$$

The electron density is obtained through the densities of all positive and negative ions under the assumption of quasi-neutrality as

$$\sum_+ n_+ = \sum_- n_- \quad (5)$$

4. Transport Equations for Neutral Species

The general continuity equation for the neutral species, assuming a diffusion dominated flow under the low-pressure condition, is written as

$$\frac{\partial n_k}{\partial t} + \nabla \cdot (-D_k \nabla n_k) = R_{k,\text{source}} - R_{k,\text{sink}} \quad (6)$$

where n_k is the k th neutral density, $R_{k,\text{source}}$ and $R_{k,\text{sink}}$ are the source and sink terms of the k th neutral species, respectively, resulting from chemical reactions, and D_k is the diffusion coefficient of the k th neutral species in a mixture of background gas. The diffusion coefficients are obtained by the Blancs law with the binary diffusion coefficients calculated using the Chapman-Enskog kinetic equation.^[37] The boundary conditions of the neutral continuity equations are set as zero gradients at the axis of symmetry and a thermal flux of $1/4n_k \sqrt{8k_B T_g / \pi M_k}$ at the surface, and the ions are neutralized at all solid boundaries. Note T_g and M_k are the background gas temperature and molecular weight of species k . For non-radical (or non-reactive) neutral species, we have assumed they fully reflected back into the chamber, which makes the density gradient vanishes at the wall. For radical (reactive) neutral species, the reflected fluxes depend on the surface reactions occurring at the different types of walls (quartz window, SiO₂ substrate, and metal). The inflow boundary condition considers the feedstock gas and the outflow boundary condition considers an iterative (or adjustable) pumping speed out of the chamber, depending upon the preset chamber pressure.

5. Electromagnetic and Power Absorption

The electromagnetic field in the plasma generated by the antenna coil is obtained by solving the general vector wave equation that is derived from the Maxwell's equations. The vector wave equation can be expressed as

$$\nabla^2 \vec{E} = \mu_0 \frac{\partial \vec{J}_{\text{total}}}{\partial t} + \frac{1}{c^2} \frac{\partial^2 \vec{E}}{\partial t^2} \quad (7)$$

where c is the speed of light, μ_0 is the permeability of vacuum, and \vec{J}_{total} is the total current that can be classified into three regions, including plasma zone, quartz zone, and coil-vacuum zone, which are described next in turn. Note only azimuthal component of the electromagnetic fields needs to be considered since we assume the problem is axisymmetric. The induced electric field is driven sinusoidally by a time-varying current and, thus, the induced electric field can be described as $E_\theta(t) = \tilde{E}_\theta e^{j\omega t}$, where \tilde{E}_θ is the phasor of electric field amplitude in the azimuthal direction and ω is the frequency of applied current. Similarly, the quantity of applied current can be written in a phasor

representation ($J_\theta(t) = \tilde{J}_\theta e^{j\omega t}$). Note in Equation (7) and hereafter the subscript θ may be ignored for brevity.

In the plasma zone, the plasma can be treated as a conductor in the plasma zone and the total current density can be expressed by the Ohm's law $\vec{J}_{\text{total}} = \tilde{J}_{\text{plasma}} = \sigma_p \vec{E}$. The plasma conductivity σ_p is defined in ref.^[39]

$$\begin{aligned} \sigma_p &= \frac{\varepsilon_0 \omega_{pe}^2}{j\omega + \nu_m} = \frac{\varepsilon_0 \omega_{pe}^2 \nu_m}{\omega^2 + \nu_m^2} - j \frac{\varepsilon_0 \omega_{pe}^2 \omega}{\omega^2 + \nu_m^2} \\ &= \sigma_{p,R} + j\sigma_{p,I} \end{aligned} \quad (8)$$

where ε_0 is the vacuum dielectric constant, $\omega_{pe} = \sqrt{q^2 n_e / \varepsilon_0 m_e}$ is the plasma frequency, and ν_m is the electron-neutral collision frequency. In the quartz zone, the polarization is represented by the displacement current, which is written as

$$\vec{J}_{\text{total}} = \vec{J}_{\text{pol}} = \mu_0 \varepsilon_0 \omega^2 \varepsilon_r \vec{E} \quad (9)$$

where $\varepsilon_r (=3.8)$ is the dielectric constant of a quartz. In the coil-vacuum zone, the applied RF power drives the conduction current through the coil can be written as:

$$\vec{J}_{\text{total}} = \vec{J}_0 \quad (10)$$

where \vec{J}_0 is applied current density.

The vector wave equation can be written as, by dividing into real part and imaginary part $\vec{E}_\theta = E_{Re} + jE_{Im}$,

$$\begin{cases} \nabla^2 E_{Re} - \mu_0 \omega \sigma_{p,I} E_{Re} + \mu_0 \omega \sigma_{p,R} E_{Im} + \frac{\omega^2}{c^2} E_{Re} = 0 \\ \nabla^2 E_{Im} - \mu_0 \omega \sigma_{p,I} E_{Im} - \mu_0 \omega \sigma_{p,R} E_{Re} \\ \quad + \frac{\omega^2}{c^2} E_{Im} - \mu_0 \omega J_0 = 0 \end{cases} \quad (11)$$

We assume that electromagnetic fields vanish at the central axis due to the azimuthal symmetry. The perfect conductor boundary condition is applied at the metal surface of the reactor. The power density deposition in the model can be calculated by

$$\begin{aligned} P_{\text{abs}} &= \vec{J}(t) \cdot \vec{E}(t) = \text{Re}\{\tilde{J} e^{j\omega t}\} \text{Re}\{\tilde{E} e^{j\omega t}\} \\ &= \frac{1}{2} \int \text{Re}\{J^*(t) \cdot E(t)\} dt = \frac{1}{2} \{(\sigma_{p,R} E_{Re} + \sigma_{p,I} E_{Im}) E_{Re} \\ &\quad + (\sigma_{p,R} E_{Im} - \sigma_{p,I} E_{Re}) E_{Im}\} \end{aligned} \quad (12)$$

The input coil current is adjusted iteratively during the simulation to match the preset absorption power.

5.1. Electron Energy Density Equation

The electron energy density equation is expressed as

$$\begin{aligned} \frac{\partial n_e}{\partial t} + \nabla \cdot \vec{Q}_e &= -e \vec{\Gamma}_e \cdot \vec{E}_s - \sum_i R_{i,e} \varepsilon_{i,\text{loss}} \\ &\quad - 3 \frac{m_e}{M} n_e k_B \nu_m (T_e - T_g) + P_{\text{abs}} \end{aligned} \quad (13)$$

where $n_e = (3/2)n_e k_B T_e$ is the electron energy density, \vec{E}_s is the electrostatic field, T_e is the electron temperature, $R_{i,e}$ is the reaction rate of the i th inelastic electron collision, $\epsilon_{i,loss}$ is the energy loss of the i th inelastic electron collision, k_B is the Boltzmann constant, ν_m is the momentum exchange collision frequency between the electron (mass m_e) and the background neutral (mass M), T_g is the background gas temperature, P_{abs} is the power absorption given by Equation (12) and \bar{Q}_e is the corresponding electron energy

density flux as

$$\bar{Q}_e = \frac{5}{2} k_B T_e \bar{\Gamma}_e - \frac{5}{2} \frac{n_e k_B T_e}{m_e \nu_e} \nabla(k_B T_e) \quad (14)$$

where $\bar{\Gamma}_e$ is the electron flux obtained from Equation (4). Similarly, the boundary conditions at walls are applied considering the thermal diffusion, $\bar{Q}_e = 2k_B T_e \bar{\Gamma}_e$,^[39] and it is assumed that $\bar{Q}_e = 0$ at the axis because of symmetry.

Table 1. The overview of the species and the corresponding parameters for the transport properties.

Species	σ (Å) L.-J. parameter	ϵ (K ^o) L.-J. potential	α (Å ³) polarizability	Reference
Electron	0	0	0	N/A
F ⁺	2.968	112.6	0.6	[18]
CF ⁺	3.635	94.2	1.8	[18]
CF ₂ ⁺	3.977	108	2.82	[18]
CF ₃ ⁺	4.32	121	2.82	[18]
O ⁺	3.04	103.85	0.802	[37]
O ₂ ⁺	3.433	113.0	1.5812	[37]
CO ⁺	3.59	110.0	1.95	[37]
SiF ⁺	3.662 ^{a)}	95.8 ^{a)}	4.62 ^{c)}	[66]
SiF ₂ ⁺	3.803 ^{a)}	133.1 ^{a)}	4.62 ^{c)}	[66]
SiF ₃ ⁺	3.943 ^{a)}	170.3 ^{a)}	4.62 ^{c)}	[66]
F ⁻	2.968	112.6	0.6	[19]
O ⁻	3.04	103.85	0.802	[37]
F	2.968	112.6	0.6	[19]
CF	3.635	94.2	1.8	[19]
CF ₂	3.977	108	2.82	[19]
CF ₃	4.32	121	2.82	[19]
O	3.04	103.85	0.802	[37]
O ₂	3.433	113.0	1.5812	[37]
O(¹ D)	3.04	103.85	0.802	[37]
O ₂ (a ¹ Δ _g)	3.433	113.0	1.5812	[37]
COF	3.941 ^{b)}	195.2 ^{b)}	1.95 ^{b)}	Estimated
COF ₂	3.941 ^{b)}	195.2 ^{b)}	1.95 ^{b)}	Estimated
CO	3.59	110.0	1.95 ^{b)}	[70,71]
CO ₂	3.941	195.2	1.95 ^{b)}	[70,71]
Si	2.91	93.6231	5.38	[70]
SiF	3.662 ^{a)}	95.8 ^{a)}	5.38	[70]
SiF ₂	3.803 ^{a)}	133.1 ^{a)}	5.38	[70]
SiF ₃	3.943 ^{a)}	170.3 ^{a)}	5.38	[70]
SiF ₄	4.084 ^{a)}	207.6 ^{a)}	5.45	[70]
F ₂	3.357	112.6	0.9	[19]
CF ₄	4.662	134	2.82	[19]

^{a)}Estimate based on SiH_x analogy. ^{b)}Estimate based on CO or CO₂. ^{c)}Estimate based on SiH_x⁺ analogy.

5.2. Gas-Phase Reactions

To properly model the gas-phase etching products in a tetrafluoromethane discharge, we have extended the gas-phase reactions proposed for a CF₄ discharge^[19] by adding the related reactions of etching reactants, such as the oxygen-containing species and the tetrafluorosilane species. In addition, the gas phase chemistry reactions related to the etching products O₂ and SiF_x are also taken into account in the model.^[35,37,40] It is generally very difficult to dissociate CF₄ into C (and thus C₂) directly since it needs to go through a series of dissociative reactions that rarely occurs. This is also confirmed by the experimental observation in a CF₄ ICP reactor,^[41] under similar test conditions, in which only an extremely small amount of “C”

was found. Thus, we have neglected these species in our fluid modeling. Table 1 summarizes an overview of all the species considered in the simulation along with their corresponding Lennard-Jones parameters and polarizabilities which were used for calculating the transport properties. The total number of species is 32, which include the electron, F⁺, CF_x⁺ (x = 1–3), O⁺, O₂⁺, CO⁺, SiF_x⁺ (x = 1–3), F[−], O[−], F, CF_x (x = 1–4), F₂, O, O₂, CO, CO₂, COF, COF₂, Si, and SiF_x (x = 1–4). Table 2 lists the reactions of electron impact with CF_x (x = 1–4) and related gas-phase reactions involving CF_x (x = 1–4), in which the cross section are referred to Christophorou et al.,^[42] Lennon et al.,^[43] Tarnovsky et al.,^[44] and Center and Mandl.^[45] Table 3 lists the reactions related to the negative charged fluoride F[−], in which the cross section data are obtained from Christophorou

Table 2. The reactions of the electron impacts with CF_x (x = 1–4) and the relative gas-phase reactions.

Index	Reaction	Threshold energy (eV)	Rate constant (m ³ s ^{−1})	Ref.
F00	e + CF ₄ → CF ₄ + e	0	EEDF (σ)	[42]
F01	e + CF ₃ → CF ₃ ⁺ + 2e	9.09	EEDF (σ)	[42]
F02	e + CF ₂ → CF ₂ ⁺ + 2e	11.5	EEDF (σ)	[42]
F03	e + CF → CF ⁺ + 2e	9.17	EEDF (σ)	[42]
F04	e + F → F ⁺ + 2e	17.5	EEDF (σ)	[43]
F05	e + CF ₄ → CF ₃ ⁺ + F + 2e	14.8	EEDF (σ)	[42]
F06	e + CF ₄ → CF ₂ ⁺ + 2F + 2e	20.8	EEDF (σ)	[42]
F07	e + CF ₄ → CF ⁺ + 3F + 2e	23.9	EEDF (σ)	[42]
F08	e + CF ₃ → CF ₂ ⁺ + F + 2e	15.2	EEDF (σ)	[42,44]
F09	e + CF ₃ → CF ⁺ + 2F + 2e	18.2	EEDF (σ)	[42,44]
F10	e + CF ₂ → CF ⁺ + F + 2e	14.6	EEDF (σ)	[42,44]
F11	e + CF ₄ → CF ₃ + F + e	5.67	EEDF (σ)	[42]
F12	e + CF ₄ → CF ₂ + 2F + e	9.32	EEDF (σ)	[42]
F13	e + CF ₄ → CF + 3F + e	14.7	EEDF (σ)	[42]
F14	e + CF ₃ → CF ₂ + F + e	3.65	EEDF (σ)	[44]
F15	e + CF ₃ → CF + 2F + e	9.04	EEDF (σ)	[44]
F16	e + CF ₂ → CF + F + e	5.39	EEDF (σ)	[44]
F17	e + F ₂ → F + F + e	1.65	EEDF (σ)	[45]
F18	e + CF ₃ ⁺ → CF ₂ + F	−5.44	6.0 × 10 ^{−14}	[18]
F19	e + CF ₂ ⁺ → CF + F	−6.1	6.0 × 10 ^{−14}	[18]
F20	e + CF ₃ ⁺ → CF ₃	−8.5	4.0 × 10 ^{−14}	[18]
F21	CF ₃ + F ₂ → CF ₄ + F	0	1.5 × 10 ^{−20}	[18]
F22	CF ₂ + F ₂ → CF ₃ + F	0	8.3 × 10 ^{−20}	[18]
F23	CF ₄ + CF ₃ + F → 2CF ₄	0	1.47 × 10 ^{−40}	[60]
F24	CF ₄ + CF ₂ + F → CF ₃ + CF ₄	0	1.42 × 10 ^{−41}	[60]
F25	CF + F → CF ₂	0	1.0 × 10 ^{−19}	[60]
F26	F ⁺ + CF ₃ → F + CF ₃ ⁺	0	6.0 × 10 ^{−15}	[18]
F27	F ⁺ + CF ₄ → F ₂ + CF ₃ ⁺	0	6.0 × 10 ^{−15}	[18]

Table 3. The reactions that relate to the negative ion F^- .

Index	Reactions	Threshold energy	Rate constant ($m^3 s^{-1}$)	Ref.
FN01	$e + CF_4 \rightarrow CF_3 + F^-$	2.21	EEDF (σ)	[42]
FN02	$e + CF_3 \rightarrow CF_2 + F^-$	0.18	EEDF (σ) ^a	[42]
FN03	$e + CF_2 \rightarrow CF + F^-$	1.93	EEDF (σ) ^a	[42]
FN04	$e + F_2 \rightarrow F + F^-$	-1.82	EEDF (σ) ^a	[46]
FN05	$e + CF_4 \rightarrow CF_3^+ + F^- + e$	11.3	EEDF (σ)	[42]
FN06	$e + CF_3 \rightarrow CF_2^+ + F^- + e$	11.7	EEDF (σ)	[42]
FN07	$e + F^- \rightarrow F + 2e$	3.47	$5.456 \times 10^{-16} T_e^{1.175} \exp(-3.296/T_e)$	[18]
FN08	$CF_3 + F^- \rightarrow CF_4 + e$	-2.21	5.0×10^{-16}	[18]
FN09	$CF_2 + F^- \rightarrow CF_3 + e$	-0.18	5.0×10^{-16}	[18]
FN10	$CF + F^- \rightarrow CF_2 + e$	-1.93	5.0×10^{-16}	[18]
FN11	$F + F^- \rightarrow F_2 + e$	1.82	1.39×10^{-16}	[18]
FN12	$CF_3^+ + F^- \rightarrow CF_3 + F$	0	8.8×10^{-13}	[18]
FN13	$CF_2^+ + F^- \rightarrow CF_2 + F$	0	8.8×10^{-13}	[18]
FN14	$CF^+ + F^- \rightarrow CF + F$	0	8.8×10^{-13}	[18]
FN15	$F^+ + F^- \rightarrow 2F$	0	4.0×10^{-13}	[35]
FN16	$CF_3^+ + F^- \rightarrow CF_4$	0	5.0×10^{-14}	[35]

et al.^[42] and Morgan.^[46] Table 4 summarizes the reactions related to the electron-impact and the gas-phase reactions of oxygen containing species, in which the cross-section source are from Itikawa et al.,^[47–50] Eliasson et al.^[51], and Rapp and Englander-Golden^[52] Table 5 lists the reactions related to the electron-impact and the gas-phase reactions of the etching products SiF_x , in which the cross section data are from Basner et al.,^[53] Nakano and Sugai,^[54] Iga et al.^[55] and Hayes et al.^[56–58] In brief summary, we consider 96 gas-phase reaction channels in the fluid model.

A Boltzmann equation solver named BOLSIG+^[59] was used to calculate rate constants of electron impact reaction and electron transport coefficients on the basis of energy dependent cross sections. The electron mobility, the electron diffusivity and the rate constants of electron impact related channels are tabulated as a function of electron temperature. Through these tables, the rates, the mobility, and the diffusion coefficients related to the electrons can be computed depending on the electron temperature calculated by the electron energy density equation. In addition, the rate constants of the remaining gas-phase reactions in Table 2–4 are available in the databases like NIST^[60] and NIFS.^[61] In some cases, the rate parameters are estimated and adjusted to improve the agreement between simulations and experiments based on the physical understanding of the reaction process.

5.3. Surface Kinetic Model

In this study, we have implemented a surface kinetic model with the consideration of silicon dioxide (SiO_2) etching process based on the site balance concept. Therefore, the distribution of etching rate on the substrate in a CF_4 plasma can be obtained by incorporating the etching products into the fluid modeling. Table 6 summarizes the surface reactions of SiO_2 etching and related coefficients required for the modeling,^[2,3] in which 18 surface reactions are included. In this surface site model, fluorine (F), fluorocarbon radicals (denoted as CF_x), and surface polymer (P) consisting of clustering molecules are considered. The concept of surface “coverage,” θ ($0 \leq \theta \leq 1$), is applied to the species in the surface layer under the effects of ion and radical fluxes impinging on the substrate. The etching mechanisms considered in the surface model include: (a) physical sputtering, (b) ion-enhanced etching with F atoms and CF_x radicals, and (c) thermal etching. The etching process continues as long as the formed polymers do not occupy all the surface sites ($\theta_p < 1$). The deposition mechanisms considered in the surface model include: (a) direct ion deposition, and (b) “sticking” or “ion-enhanced deposition” of CF_x radicals on the surface. A simultaneous mechanism of the ion enhanced etching of polymer with F atoms is also considered. Therefore, the various kinds of surface coverage, including the fluorine atom (θ_F), the fluorocarbon radicals (θ_{CF_x}) and the polymer (θ_p), are

Table 4. The reactions of the electron impacts with oxygen-containing species and the relative gas-phase reactions.

Index	Reactions	Threshold energy (eV)	Rate constant (m ³ s ⁻¹)	Ref.
Ox01	$e + O \rightarrow O^+ + 2e$	13.62	EEDF (σ)	[47]
Ox02	$e + O \rightarrow O(^1D) + e$	1.97	EEDF (σ)	[47]
Ox03	$e + O(^1D) \rightarrow O^+ + 2e$	11.65	EEDF (σ)	[47]
Ox04	$e + O_2 \rightarrow O_2^+ + 2e$	12.1	EEDF (σ)	[48,49]
Ox05	$e + O_2 \rightarrow O_2(v=1) + e$	0.19	EEDF (σ)	[48,49]
Ox06	$e + O_2 \rightarrow O_2(v=2) + e$	0.38	EEDF (σ)	[48,49]
Ox07	$e + O_2 \rightarrow O_2(v=3) + e$	0.57	EEDF (σ)	[48,49]
Ox08	$e + O_2 \rightarrow O_2(v=4) + e$	0.75	EEDF (σ)	[48,49]
Ox09	$e + O_2 \rightarrow O_2(\text{Ryd}) + e$	4.5	EEDF (σ)	[48,49]
Ox10	$e + O_2 \rightarrow O_2(a^1\Delta_g) + e$	0.977	EEDF (σ)	[48,49]
Ox11	$e + O_2(a^1\Delta_g) \rightarrow O_2^+ + e$	11.16	EEDF (σ)	[51]
Ox12	$e + O_2(a^1\Delta_g) \rightarrow O^- + O$	2.66	EEDF (σ)	[51]
Ox13	$e + O_2(a^1\Delta_g) \rightarrow O_2 + e$	-0.977	EEDF (σ)	[51]
Ox14	$e + O_2(a^1\Delta_g) \rightarrow 2O + e$	4.19	EEDF (σ)	[51]
Ox15	$e + O_2(a^1\Delta_g) \rightarrow O + O^+ + 2e$	17.7	EEDF (σ)	[51]
Ox16	$e + O_2 \rightarrow 2O + e$	5.17	EEDF (σ)	[48,49]
Ox17	$e + O_2 \rightarrow O + O(^1D) + e$	7.13	EEDF (σ)	[48,49]
Ox18	$e + O_2 \rightarrow O^- + O^+ + e$	17.32	EEDF (σ)	[48,49]
Ox19	$e + O_2 \rightarrow O^- + O$	3.64	EEDF (σ)	[48,49]
Ox20	$e + O_2 \rightarrow O^+ + O + 2e$	18.84	EEDF(σ)	[48,49]
Ox21	$e + O_2^+ \rightarrow 2O$	-6.97	$5.1 \times 10^{-15} T_e$	[39]
Ox22	$e + O^- \rightarrow O + 2e$	1.53	$2.0 \times 10^{-13} \exp(-5.5/T_e)$	[35]
Ox23	$O^- + O \rightarrow O_2 + e$	-3.64	$3.0 \times 10^{-16} \times (300.0/T_g)^{0.5}$	[37]
Ox24	$O^- + O^+ \rightarrow 2O$	0	$2.7 \times 10^{-13} \times (300.0/T_g)^{0.5}$	[37]
Ox25	$O^- + O_2^+ \rightarrow O + O_2$	0	$1.5 \times 10^{-13} \times (300.0/T_g)^{0.5}$	[37]
Ox26	$e + CO_2 \rightarrow CO + O + e$	6.1	EEDF(σ)	[50]
Ox27	$e + COF_2 \rightarrow COF + F + e$	6.0	$1.13 \times 10^{-14} T_e^{-0.399} \exp(-13.1/T_e)$	[8]
Ox28	$e + CO \rightarrow CO^+ + 2e$	14.0	EEDF(σ)	[52]
Ox29	$CF_3 + O \rightarrow COF_2 + F$	0	3.1×10^{-17}	[35]
Ox30	$CF_3 + O \rightarrow COF + F$	0	1.4×10^{-17}	[35]
Ox31	$CF_2 + O \rightarrow CO + 2F$	0	4.0×10^{-18}	[35]
Ox32	$COF + O \rightarrow CO_2 + F$	0	9.3×10^{-17}	[35]
Ox33	$COF + F \rightarrow COF_2$	0	8.0×10^{-19}	[35]
Ox34	$COF + CF_2 \rightarrow CF_3 + CO$	0	3.1×10^{-19}	[35]
Ox35	$COF + CF_2 \rightarrow COF_2 + CF$	0	3.1×10^{-19}	[35]
Ox36	$COF + CF_3 \rightarrow CF_4 + CO$	0	1.0×10^{-17}	[35]
Ox37	$COF + CF_3 \rightarrow COF_2 + CF_2$	0	1.0×10^{-17}	[35]
Ox38	$COF + COF \rightarrow COF_2 + CO$	0	1.0×10^{-17}	[35]
Ox39	$CF + O \rightarrow CO + F$	0	3.0×10^{-17}	[35]

Table 5. The reactions of the electron impacts with SiF_x and the relative gas-phase reactions.

Index	Reactions	Threshold energy (eV)	Rate constant (m ³ s ⁻¹)	Ref.
SF01	e + SiF ₄ → SiF ₃ ⁺ + F + 2e	16.0	EEDF (σ)	[53]
SF02	e + SiF ₄ → SiF ₂ ⁺ + 2F + 2e	23.4	EEDF (σ)	[53]
SF03	e + SiF ₄ → SiF ⁺ + 3F + 2e	25.1	EEDF (σ)	[53]
SF04	e + SiF ₃ → SiF ₃ ⁺ + 2e	9.6	EEDF (σ)	[56]
SF05	e + SiF ₂ → SiF ₂ ⁺ + 2e	10.8	EEDF (σ)	[57]
SF06	e + SiF → SiF ⁺ + 2e	7.26	EEDF (σ)	[58]
SF07	e + SiF ₄ → F ⁻ + SiF ₃	3.8	EEDF (σ)	[55]
SF08	e + SiF ₃ ⁺ → SiF ₃	8.5	4.0 × 10 ¹⁴	[35]
SF09	e + SiF ₄ → SiF ₃ + F + e	7.25	EEDF (σ)	[54]
SF10	e + SiF ₄ → SiF ₂ + 2F + e	11.9	EEDF (σ)	[54]
SF11	e + SiF ₄ → SiF + 3F + e	18.6	EEDF (σ)	[54]
SF12	SiF ₃ ⁺ + F ⁻ → SiF ₄	0	5.0 × 10 ⁻¹⁴	[35]
SF13	SiF ₃ + F → SiF ₄	0	1.0 × 10 ⁻¹⁶	[35]
SF14	SiF ₂ + F → SiF ₃	0	1.0 × 10 ⁻¹⁶	[35]
SF15	SiF + F → SiF ₂	0	1.0 × 10 ⁻¹⁶	[35]
SF16	Si + F → SiF	0	1.0 × 10 ⁻¹⁶	[35]

considered in the surface model, which solves a set of steady-state surface site balance equations. These equations are written as:^[2]

$$\frac{d(\theta_F)}{dt} = s_F(1 - \theta_{TOT})\Gamma_F - 2\beta_F\theta_F\Gamma_{ION} = 0 \quad (15)$$

$$\frac{d(\theta_{CF_x})}{dt} = \sum_i s_{CF_i}(1 - \theta_{TOT})\Gamma_{CF_i} - \gamma_c\theta_{CF_x}\Gamma_{ION} - \beta_{CF_x}\theta_{CF_x}\Gamma_{ION} - k_{REC}\theta_{CF_x}\Gamma_F = 0 \quad (16)$$

$$\frac{d(\theta_P)}{dt} = \sum_i \chi_i \gamma_{d,i}\Gamma_{ION} + \beta_s\theta_{CF_x}\Gamma_{ION} + \beta_s\theta_P\theta_{CF_x/P}\Gamma_{ION} - \beta_{F/P}\theta_P\theta_{F/P}\Gamma_{ION} = 0 \quad (17)$$

where $\theta_{TOT} = \theta_F + \theta_{CF_x} + \theta_P$ is the sum of coverage (i.e. 1 - θ_{TOT} is uncovered area). s_F and s_{CF_x} are the sticking coefficients of F and CF_x on SiO₂ surface. β_F and β_{CF_x} are the etching coefficients of ion enhanced chemical etching by F and CF_x, respectively. $\beta_{F/P}$ and β_s are the etching coefficients of ion enhanced etching of polymer by F and ion enhanced deposition of radicals, respectively. γ_c and $\gamma_{d,i}$ are the etching yields for the sputtering and the direct ion deposition, respectively. χ_i denotes the ratio of the *i*th ion flux to the total ion flux. Moreover, Γ_F , Γ_{ION} , and Γ_{CF_i} are the F atom flux, the total ion flux and the fluorocarbon flux, respectively. Besides, the F and CF_x react not only with the SiO₂ surface but also with the polymer layer. The surface

coverage ratios for the F and CF_x on the polymer surface are denoted as $\theta_{F/P}$ and $\theta_{CF_x/P}$, respectively, expressed in a similar manner.^[2]

$$\frac{d(\theta_{F/P})}{dt} = s_{F/P}(1 - \theta_{TOT/P})\Gamma_F - \beta_{F/P}\theta_{F/P}\Gamma_{ION} = 0 \quad (18)$$

$$\frac{d(\theta_{CF_x/P})}{dt} = \sum_i s_{CF_i/P}(1 - \theta_{TOT/P})\Gamma_{CF_i} - \gamma_c\theta_{CF_x}\Gamma_{ION} - \beta_{CF_x/P}\theta_{CF_x/P}\Gamma_{ION} - k_{REC}\theta_{CF_x/P}\Gamma_F = 0 \quad (19)$$

where $\theta_{TOT} = \theta_{F/P} + \theta_{CF_x/P}$. Because the treatments of site balance for $\theta_{F/P}$ and $\theta_{CF_x/P}$ on the polymer surface are similar to those of θ_F and θ_{CF_x} on SiO₂, they are listed in Table 6 for reference.^[2,3] In this study, the surface model is used to estimate the etching products and the etching rate through the calculation of radical and neutral fluxes depleted from the SiO₂ surface. When the incident fluxes of F, CF_x, and ions are determined by fluid model, the surface site coverage ratios can be obtained via solving site balance Equation (15)–(19). These coverage ratios are then employed to determine the net fluxes of etching products generated from SiO₂ entering into gas phase. Before the etching rate is calculated, the flux of etching yield is estimated as^[2]

$$\Gamma_{Y_{SiO_2}} = \sum_i \chi_i \gamma_{SP,i}(1 - \theta_{TOT})\Gamma_{ION} + \beta_F\theta_F\Gamma_{ION} + \beta_{CF_x}\theta_{CF_x}\Gamma_{ION} + k_{rec}(1 - \theta_{CF_x} - \theta_P)\Gamma_F \quad (20)$$

Table 6. The surface reactions of the SiO₂ etching and related coefficients.

No.	Reaction	Process	Flux dependency	Surface coverage	Rate coefficient
Physical sputtering					
S1	SiO ₂ (s) → Si(g) + 2O(g)	Physical sputtering	Γ _{ion}	1 - θ _{TOT}	γ _{SP}
Reactions with F atoms					
S2	SiO ₂ (s) + 2F(g) → SiO ₂ F ₂ (s)	Adsorption	Γ _F	1 - θ _{TOT}	S _F
S3	SiO ₂ F ₂ (s) + 2F(s) → SiF ₄ (g) + O ₂ (g)	Ion-enhanced chemical etching by F	Γ _{ion}	θ _F	β' _F
S4	SiO ₂ F ₂ (s) → SiF ₂ (g) + O ₂ (g)	Ion-enhanced chemical sputtering	Γ _{ion}	θ _F	β' _F b
S5	SiO ₂ F ₂ (s) + 2F(g) → SiF ₄ (g) + O ₂ (g)	Thermal etching by F	Γ _F	1 - θ _{CF} - θ _P	K(T)
Reactions with CF _x (x = 1–3)					
S6	SiO ₂ (s) + CF _x (g) → SiO ₂ CF _x (s)	Chemisorption	Γ _{CF_x}	1 - θ _{TOT}	S _{CF_x}
S7	2SiO ₂ CF _x (s) → SiF _x (g) + 2CO(g) + SiO ₂ F _x (s)	Ion-enhanced chemical etching by CF _x radicals	Γ _{ion}	θ _{CF_x}	β _{CF_x}
S8	2SiO ₂ CF _x (s) → Si(s) + 2COF _x (g) + SiO ₂ (s)	C sputtering	Γ _{ion}	θ _{CF_x}	γ _C
S9	SiO ₂ CF _x (s) + F(g) → SiO ₂ (s) + CF _{x+1} (g)	Recombination of CF _x with F	Γ _F	θ _{CF_x}	k _{REC}
Reactions of polymer production of loss					
S10	CF _x ⁺ (g) → P	Direct ion deposition	Γ _{ion}	1	γ _d
S11	SiO ₂ CF _x (s) → P	Ion-enhanced deposition of sorbed radicals	Γ _{ion}	θ _{CF_x}	β _S
S12	P-F(s) → etching of P	Ion-enhanced etching of polymer by F atoms	Γ _{ion}	θ _P θ _{F/P}	β _{F/P}
S13	P-CF _x (s) → more P	Ion-enhanced deposition of sorbed radicals	Γ _{ion}	θ _P θ _{CF_x/P}	β _S
Reactions with F atoms on polymer surfaces					
S14	P + 2F(g) → P-F ₂ (s)	Adsorption	Γ _F	θ _P (1 - θ _{TOT/P})	S _{F/P}
S15	P-F ₂ (s) + 2F(s) → CF ₄ (g) + O ₂ (g)	Ion-enhanced chemical etching by F	Γ _{ion}	θ _P θ _{F/P}	β _{F/P}
Reactions with fluorocarbon radicals on polymer surfaces					
S16	P(s) + CF _x (g) → P-CF _x (s)	Chemisorption	Γ _{CF_x}	θ _P (1 - θ _{TOT/P})	S _{CF_x/P}
S17	2P-CF _x (s) → 2P(s) + 2CF _x (g)	C sputtering	Γ _{ion}	θ _P θ _{CF_x/P}	γ _C
S18	PCF _x (s) + F(g) → P(s) + CF _{x+1} (g)	Recombination of CF _x with F	Γ _F	θ _P θ _{CF_x/P}	k _{REC}

where $\gamma_{SP,i}$ is the etching coefficient of physical sputtering. After the etching yield is determined, the etching rate can be calculated by

$$\text{Etching rate} = \Gamma \gamma_{SiO_2} / \sigma_{SiO_2} \quad (21)$$

where σ_{SiO_2} is the density of SiO₂, and is taken as $2.64 \times 10^{28} \text{ m}^{-3}$. Since the flux of F is always much larger than those of CF_x and ions, the mechanism of surface reactions must be an etching process (i.e. $\theta_P \ll 1$), and the SiO₂ deposition yield does not occur in the simulation. In addition, Table 7 also summarizes the list of surface

reactions at metal walls based on a concept of sticking coefficients, in which 30 reaction processes are considered.^[17,62]

5.4. Numerical Schemes and Algorithms

We have discretized the modeling equations using the finite-difference scheme, in which we have used the backward Euler method for time integration and the central-difference scheme for all spatial derivatives involved. We simply employed the central-difference scheme for the drift-diffusion flux approximation mainly because

Table 7. The surface reactions based on the stick coefficients on the metal surface.

No.	Reactions	Reaction probability	Ref.
Reactions of fluorocarbons			
W1	$F^+(g) \rightarrow F(g)$	1.0	[35]
W2	$CF^+(g) \rightarrow CF(g)$	1.0	[35]
W3	$CF_2^+(g) \rightarrow CF_2(g)$	1.0	Assumed
W4	$CF_3^+(g) \rightarrow CF_3(g)$	1.0	[35]
W5	$CF_3(g) \rightarrow CF_3(w)$	0.05	[35]
W6	$F(g) \rightarrow F(w)$	0.02	[35]
W7	$F_2(g) \rightarrow F_2(w)$	0	Assumed
W8	$CF(g) \rightarrow CF(w)$	0.2	[35]
W9	$CF_2(g) \rightarrow CF_2(w)$	0.05	[35]
W10	$CF_3(g) \rightarrow CF_3(w)$	0.05	[35]
W11	$CF_4(g) \rightarrow CF_4(w)$	0	Assumed
Reactions of oxygen-containing species			
W12	$O^+(g) \rightarrow O(g)$	1.0	[37]
W13	$O_2^+(g) \rightarrow O_2(g)$	1.0	[37]
W14	$CO^+(g) \rightarrow CO(g)$	1.0	[37]
W15	$O(g) \rightarrow 0.5O_2(g)$	0.4	[37]
W16	$O_2(g) \rightarrow O_2(w)$	0	Assumed
W17	$O(^1D) \rightarrow O(g)$	1.0	Assumed
W18	$O_2(a^1\Delta_g)(g) \rightarrow O_2(g)$	0.007	Assumed
W19	$CO(g) \rightarrow CO(w)$	0.01	Assumed
W20	$CO_2(g) \rightarrow CO_2(w)$	0.01	Assumed
W21	$COF(g) \rightarrow COF(w)$	0.01	Assumed
W22	$COF_2(g) \rightarrow COF_2(w)$	0.01	Assumed
Reactions of silicon fluorides			
W23	$SiF^+(g) \rightarrow SiF(g)$	1.0	[35]
W24	$SiF_2^+(g) \rightarrow SiF_2(g)$	1.0	[35]
W25	$SiF_3^+(g) \rightarrow SiF_3(g)$	1.0	[35]
W26	$Si(g) \rightarrow Si(w)$	0.2	[35]
W27	$SiF(g) \rightarrow SiF(w)$	0.2	[35]
W28	$SiF_2(g) \rightarrow SiF_2(w)$	0.02	[35]
W29	$SiF_3(g) \rightarrow SiF_3(w)$	0.05	[35]
W30	$SiF_4(g) \rightarrow SiF_4(w)$	0	Assumed

we have not modelled the sheath self-consistently. Instead, we have assumed ambipolar transport in the bulk (because of very thin sheath) and replaced the sheath effect by Bohm velocity in the modeling like the other researchers in the field.^[35,37,38] All the discretized equations were solved semi-implicitly (with most updated information) and sequentially at each time step. In this study, a multi-scale

time-marching approach is adopted to reduce the computational cost. For the charged species including the electron and ions, we have employed a smaller time step because the electron is very light and the electric field is decided by the distribution of the charged species densities and fluxes. In contrast, we have employed a much larger time step for those neutral species to save the computational requirement for reaching the quasi-steady state of the discharge.

Accordingly, the set of nonlinear coupled partial differential equations, including the Maxwell's equation, the electron energy density equation, the species transport, and the surface kinetic model, were recast into a linear algebraic system as $\mathbf{Ax} = \mathbf{b}$ at each time step, where \mathbf{A} denotes the matrix representation of a linear operator, \mathbf{b} is the right-hand-side vector, and \mathbf{x} is the solution vector. Since the rate of convergence of iterative Krylov projection method for particular linear system depends on its spectra, preconditioning is typically required to alter the spectra to accelerate convergence rate. Thus, we have employed the combination of iterative Krylov subspace method and a preconditioning technique to solve this matrix system.^[63]

In this study, we have tested two types of Krylov subspace methods, which include generalized minimal residual method (GMRES), and biconjugate gradient method (BCGS). As for the preconditioning, we have tested successive over-relaxation (SOR), block Jacobi method (BJACOBI), additive Schwarz methods (AMS), and LU decomposition (LU). The above matrix formation and solution are parallelized using domain decomposition through a set of parallel libraries named PETSc^[64] based on the message passing interface (MPICH).^[65]

5.5. Numerical Procedures

The simulation begins by solving the Maxwell's equations to obtain the electromagnetic fields and power deposition from a specified coil current that induces the azimuthal electric field. Through the electron energy density equation, the spatial distribution of electron temperature is then obtained for calculating the electron related transport properties, the rate constants, and the source/sink through a prepared lookup table as mentioned earlier. Then, the ion and neutral continuity equations are solved in sequence using the most updated plasma properties to obtain the instantaneous spatial distributions of concentrations ions and neutrals. Then, the electron density is obtained from the quasi-neutrality assumption. Meanwhile, the etching products depleted from SiO_2 etching into gas phase are obtained by solving the surface kinetic model (site balance equations). In turn, the effective plasma conductivity is recalculated using the most updated electron density. All the discretized equations are solved semi-implicitly and sequentially at each time step. The simulation continues until the quasi-steady state solution is obtained.

6. Results and Discussion

6.1. Validation of the Developed Parallel Fluid Modeling Code

We compare the present simulation results with the simulation and experiment performed by Fukumoto et al.^[35] in a typical cylindrical ICP chamber. The plasma reactor is 30 cm in diameter and 9 cm in height. The dielectric window is at the top with five turns of coil above it and the wafer is 20 cm in diameter at the bottom of the chamber. The major operating conditions include: a driving frequency of 13.56 MHz, a gas pressure of 20 mTorr, an input power of 250 W, and a gas flow rate of 200 sccm. In addition, an exact solution of Maxwell's equation based on the Biot-Savart's law was used as the boundary condition at the plasma-dielectric window interfaces in ref.^[35] Figure 2 shows the ion concentrations which are averaged over the entire region of the chamber, which the trend and concentrations of CF_x⁺ (x = 1–3) ions are consistent with the experiment performed by Fukumoto et al.^[66] Moreover, the distributions of other species in the chamber also agree reasonably well comparing with the simulation by Fukumoto et al.,^[35] although they are not shown in this paper. Thus, we can conclude that the current fluid modeling code is valid at least in these conditions as simulated and measured by Fukumoto et al.^[35]

6.2. Parallel Performance

Table 8 summarizes the computational time of the present parallel fluid modeling code for the CF₄ ICP with a grid size of

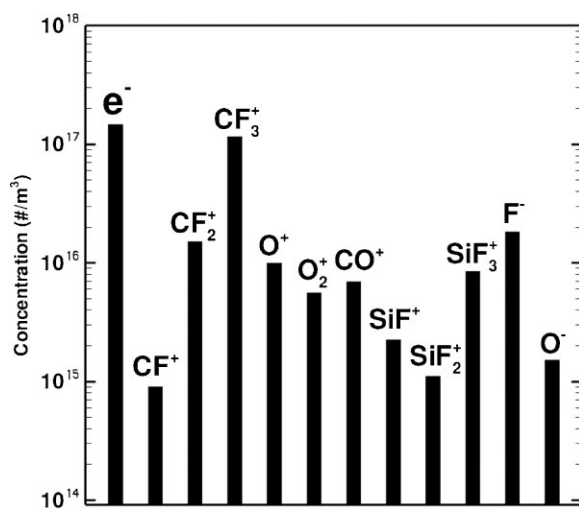


Figure 2. The spatially averaged concentration of ions in a CF₄ ICP discharge reactor. The simulation conditions refer to those used by Fukumoto et al.,^[35] in which the driving frequency is 13.56 MHz, the gas pressure is 20 mTorr, the input power is 250 W, and the gas flow rate is 200 sccm.

Table 8. The consuming time using GMRES and different combination of preconditioners and sub-preconditioners with 700 000 unknowns in 2 000 steps.

# of processors	Preconditioner + Subdomain preconditioner		
	ASM + ILU	Block Jacobi + ILU	ASM + SOR
1	8369.46	7971.88	7127.92
2	4184.73	3985.94	3563.96
4	2458.29	2361.78	2469.02
8	979.14	875.44	847.24
16	440.43	410.65	442.28
24	324.01	288.46	311.6
32	309.57	279.59	311.99

122 × 179 cells and 32 species leading to about totally 700 000 unknowns. 2 000 time steps in total was run throughout the tests using the Generalized Minimal Residual Method (GMRES) as the linear equation solver combining with various preconditioning techniques, including the Additive Schwarz Method (ASM) and the block Jacobi, on an IBM-1350 clusters at NCHC (National Center for High-Performance Computing) of Taiwan. Note each node of the IBM-1350 features Intel X5450 Processor 3.0 GHz Quad core of a CPU with 16 GB of RAM. Figure 3 shows the corresponding parallel performance as that summarized in Table 8. Results indicate that the use of

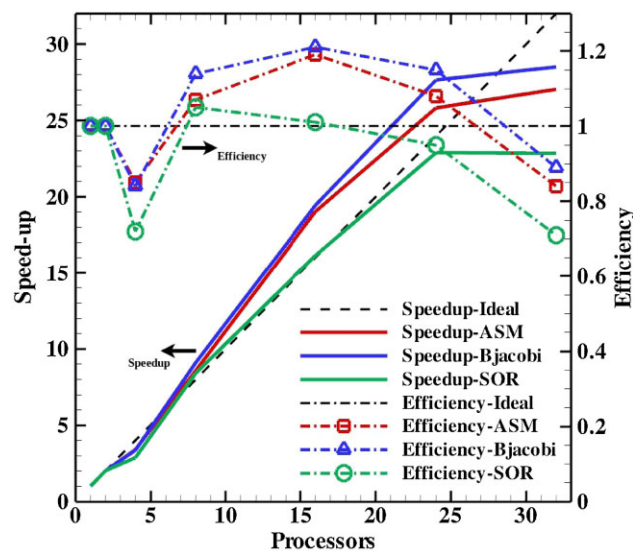


Figure 3. The speedup and parallel efficiency as a function of processor using the GMRES for the Krylov subspace method with different combinations of the preconditioner and linear matrix solver.

combination of the GMRES and the block Jacobi (or ASM) using the ILU (Incomplete lower-upper) method as the subdomain preconditioner gives the best performance and is scalable up to 26 processors. However, because there are 4 cores in each node of IBM-1350 with restricted memory, the performance is not as good as the ideal value using four processors directly. In addition, we do not show the cases with the use of subdomain preconditioner LU (Lower Upper) combining with GMRES because it is generally more costly than the ILU since the grain size is large in the current test case with less number of processors. In brief summary, we can reduce greatly the runtime at least 10–20 times using the developed fluid modeling code for studying the complex plasma physics and chemistry in a typical ICP chamber in the current study.

6.3. CF₄ Discharge in GECRC

Figure 4 shows the schematic diagram of the GECRC we have employed for the simulation of a CF₄ ICP discharge. There are four turns of coil insulated from the plasma by a quartz window (1.2 cm in thickness and 16 cm in diameter), which are driven by a current with a radio frequency (RF) of 13.56 MHz that induces electric field heating in the azimuthal direction. A wafer substrate is located at the

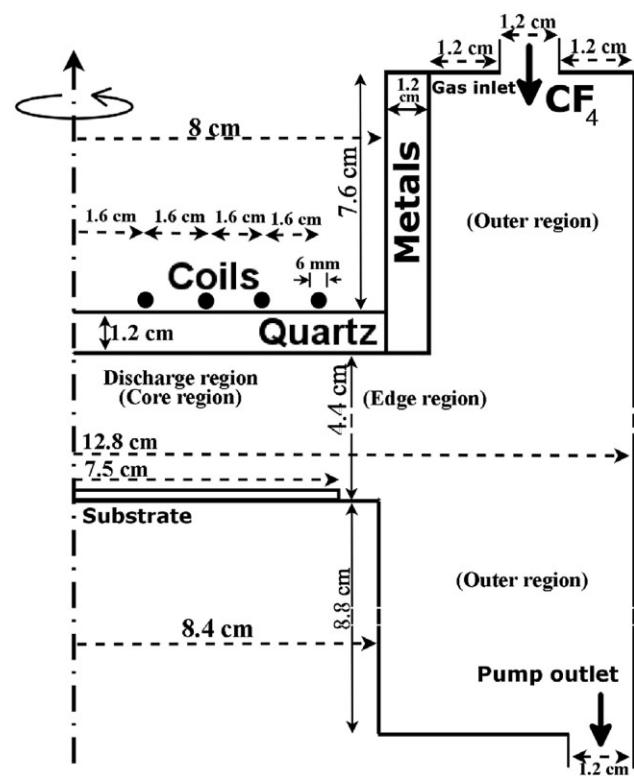


Figure 4. The schematic diagram of the cylindrical GECRC reactor for etching SiO₂.

central bottom of the reactor. A gas inlet ring for the feedstock gas, CF₄, is located along the circumferential outer top of chamber, and the pumping port is arranged at the outer bottom portion of the chamber.

The test conditions for the CF₄ ICP discharge simulation in a GECRC include: a gas pressure of 30 mTorr, a CF₄ flow rate of 150 sccm, and a preset deposited power of 150 W. The grid convergence tests confirmed that a grid of 66 × 113 cells is sufficient for obtaining essentially the same numerical solution. The temperatures of ion and neutral species are assumed to be the constant values of 0.026 eV and 400 K, respectively. The ion bombardment energy is set to be 100 eV at the substrate and 20 eV on the quartz windows. The results are compared to the experimental data wherever available. In the discussion below, the “core region” and “edge region” refer to the spatial region of the central and edge spaces, respectively, between the quartz window and the substrate. The “outer region” refers to the cylindrical space surrounding the parallel plates.

6.3.1. Spatial Distributions of Induced Electric Field

Figure 5a and 5b show the real and imaginary parts of the induced electric field in the azimuth direction, respectively. In addition, Figure 5c shows the power deposition through the ohmic heating of electrons. The real part of the electric field caused by the plasma shows a maximum intensity of about 50 V m⁻¹ in the core region where the electron temperature is as high as 3.4 eV. The imaginary part of the induced electric field caused by the coil current shows a maximum value of about 1500 V m⁻¹ near the coils and about 500 V m⁻¹ in the gas phase, and it decays rapidly by an order of magnitude within several centimeters into the high density plasma as expected. The total induced electric field is obtained from the magnitude of the complex induced electric field which is given by $|\vec{E}| = \sqrt{E_{re}^2 + E_{im}^2}$, which indicates that the total induced electric field by the coils is dominant in the core region very near the coil, while the electric field induced by the plasma can be appreciable up to 10–20% in the core region away from the coils. Therefore, the absorption of inductive power is deposited mainly by the imaginary part of the induced electric field within a few centimeters of dielectric roof. In this case, the plasma conductivity is maximal in the bulk plasma and decays towards the quartz, while the electric field is maximal at the dielectric and decays towards the plasma. The power deposition of the plasma is thus strongly related to the square of the imaginary part of electric field. Therefore, the peak power deposition is approximately 1.5 W at 1 cm below the quartz, while the power deposition becomes 0.2 W at 2.5 cm away from the quartz in the core region. Figure 5d illustrates the distribution of electron temperature in the chamber, which is strongly correlated with the distribution of power absorption as presented in

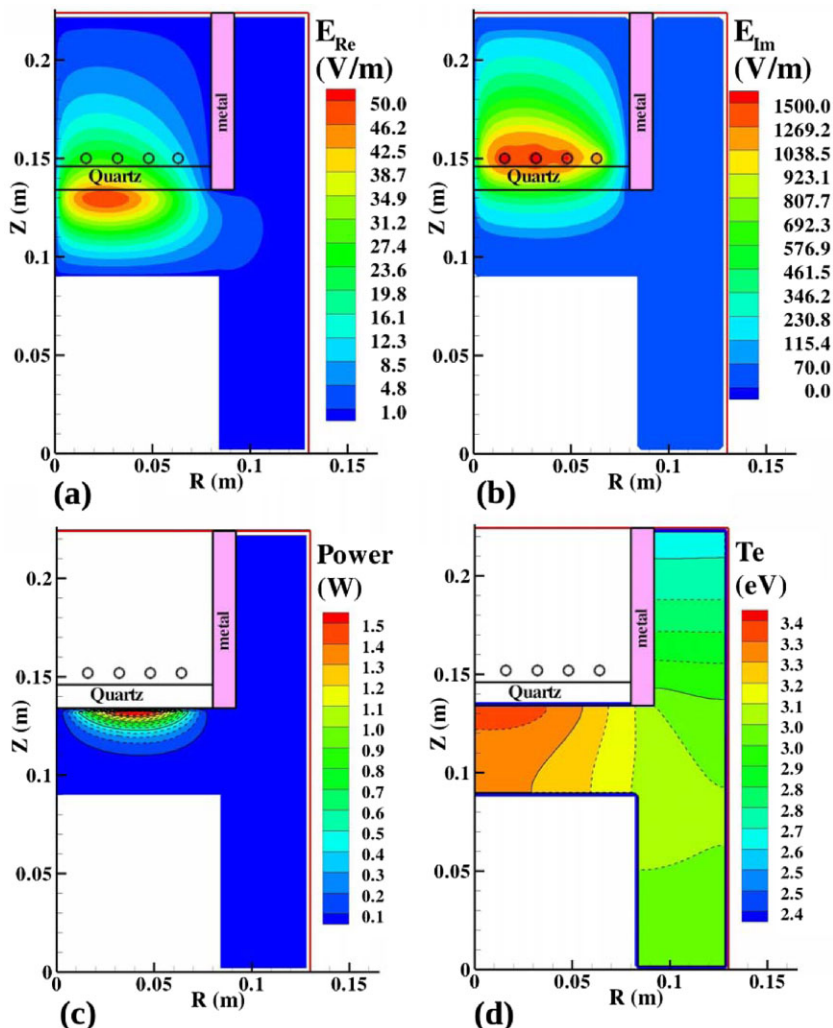


Figure 5. The two-dimensional contours of a) the real part of the induced electric field, b) the imaginary part of the induced electric field, c) the electron temperature T_e , and d) the power density.

Figure 5c. The electron temperature is the highest near the coils in the core region where the power deposition is the largest. Although the power absorption is maximal in the confined region near the dielectric window, the electron thermal conduction under the low pressure environment assists in heating up the whole plasma.

6.3.2. Field Spatial Distributions of Production Rate of Electron with CF_x ($x = 2-4$) and F₂

Figure 6a illustrates the clear depleting profile of the feeding gas CF₄ from the gas inlet to the gas outlet, which is mostly consumed by the electron collisions and pumping at the reactor outlet. Figure 6b presents the production rate of momentum transfer that the electron elastically impact with the background feedstock gas CF₄. The results show

that there are two regions having high production rates, which include the core region where the electron has a high concentration, and the gas inlet region where the CF₄ concentration is high.

Figure 7 shows a series of dissociative reactions of CF₄ caused by electron impact. Firstly, Figure 7a–c shows the production rates of F and various kinds of CF_x⁺ ($x = 3, 2, 1$) caused by the dissociative ionization by the electron impact. In Figure 7a, it shows that the dissociative ionization reaction $e + \text{CF}_4 \rightarrow 2e + \text{CF}_3^+ + \text{F}$ contributes for more than 90% of the electron and CF₃⁺ generations because its threshold energy (14.8 eV) is much lower than the threshold energies in the other reactions that produce CF₂⁺ (20.8 eV) and CF⁺ (23.9 eV). Even though these dissociative ionizations that produce CF₂⁺ and CF⁺ are not the dominant processes in a CF₄ discharge, they have

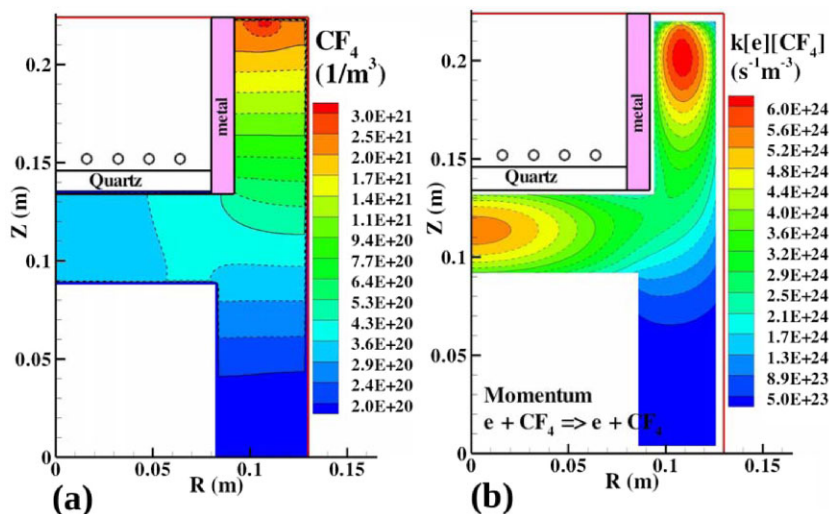


Figure 6. The two-dimensional contours of a) the feeding gas CF_4 in a unit of m^{-3} , and b) the production rate for momentum transfer reaction (Foo) in unit of $\text{m}^{-3}\text{s}^{-1}$.

significant influence on the production of F in the core region as shown in Figure 7b and 7c. Secondly, Figure 7d–f shows the production rates of F and various kinds of CF_x ($x = 3, 2, 1$) caused by the dissociation due to the electron impact. The results show that the production rates of CF_x ($x = 1–3$) and F decrease with decreasing x because of increasing dissociative threshold energy (CF_3 : 5.67 eV, CF_2 : 9.32 eV and CF : 14.7 eV). Figure 8 shows the production rates of CF_x ($x = 1–3$) and F along with F^- caused by the electron impact on CF_4 , CF_3 , CF_2 , and F_2 , respectively. We find that the dissociative attachment of CF_4 (Figure 8a) is the most dominant process in producing F^- in the discharge. This type of dissociative attachment reaction enhances the production of F^- at the cost of destroying the electrons, which leads to a high concentration of F^- in the outer region near gas inlet due to the relatively low threshold energy of attachment that will be shown next.

6.3.3. Spatial Distributions of Number Densities of Electron and Negative Charged Ions

Figure 9a and 9b show the spatial distributions of the number densities of electron and negative charged species F^- with an absorption power of 150 W at a pressure of 30 mTorr. The electron density is found to be at a peak value of $2.5 \times 10^{17} \text{m}^{-3}$ in the center of core region where the electron is produced abundantly by the attachment ionization and the dissociative ionization (F01~F10 in Table 2) by the energetic electron impact in this region (Figure 5d). Most of the electrons are lost by the diffusion to the chamber walls and few of them are lost by dissociative attachments of CF_3 and CF_4 that produce negative ions F^- (FN01~FN03 in Table 3). In addition, the static electric field

confines the electron in the center of the core region, and the electron density decreases outward as a consequence of the above-mentioned factors. The F^- concentration is found to be at a peak value of $4 \times 10^{16} \text{m}^{-3}$ at the feedstock gas inlet region and becomes two times lower in the core region because of the ion recombination process (e.g. FN16 in Table 3) where the CF_3^+ concentration peaks (Figure 7a). The current predicted data of electron and F^- agree reasonably well with the measurements by Rao et al.^[31] The F^- ions are mainly produced from two reaction paths: one is the dissociative attachment of CF_4 , and the other is the dissociative attachment of CF_3 which is dissociated from CF_4 near the feedstock gas inlet due to the lower dissociative threshold energy. For another negative ion O^- , most of the O^- is generated by the dissociative electron attachment from O_2 (Ox18 and Ox19 in Table 4). Again, it is found that the O^- concentration peaks at the center of core region because of a high concentration of electron existing in this region. We do not present it here because of its very low concentration in the order of 10^{13}m^{-3} . In general, all the negative ions are related to reactions, which are either the attachment or the recombination of the negative and positive charged species.

6.3.4. Spatial Distribution of Number Densities of Positive ions

Figure 10 shows the spatial distribution of the concentrations of positive ions including F^+ , CF^+ , CF_2^+ , and CF_3^+ . Results show that these species concentrated in the central core region due to electron related ionization from feedstock gas CF_4 (F01~F10) with $\text{CF}_3^+ (\sim 2 \times 10^{17} \text{m}^{-3}) > \text{CF}_2^+ (\sim 4 \times 10^{16} \text{m}^{-3}) > \text{CF}^+ (\sim 1 \times 10^{16} \text{m}^{-3}) > \text{F}^+ (\sim 1 \times 10^{14} \text{m}^{-3})$,

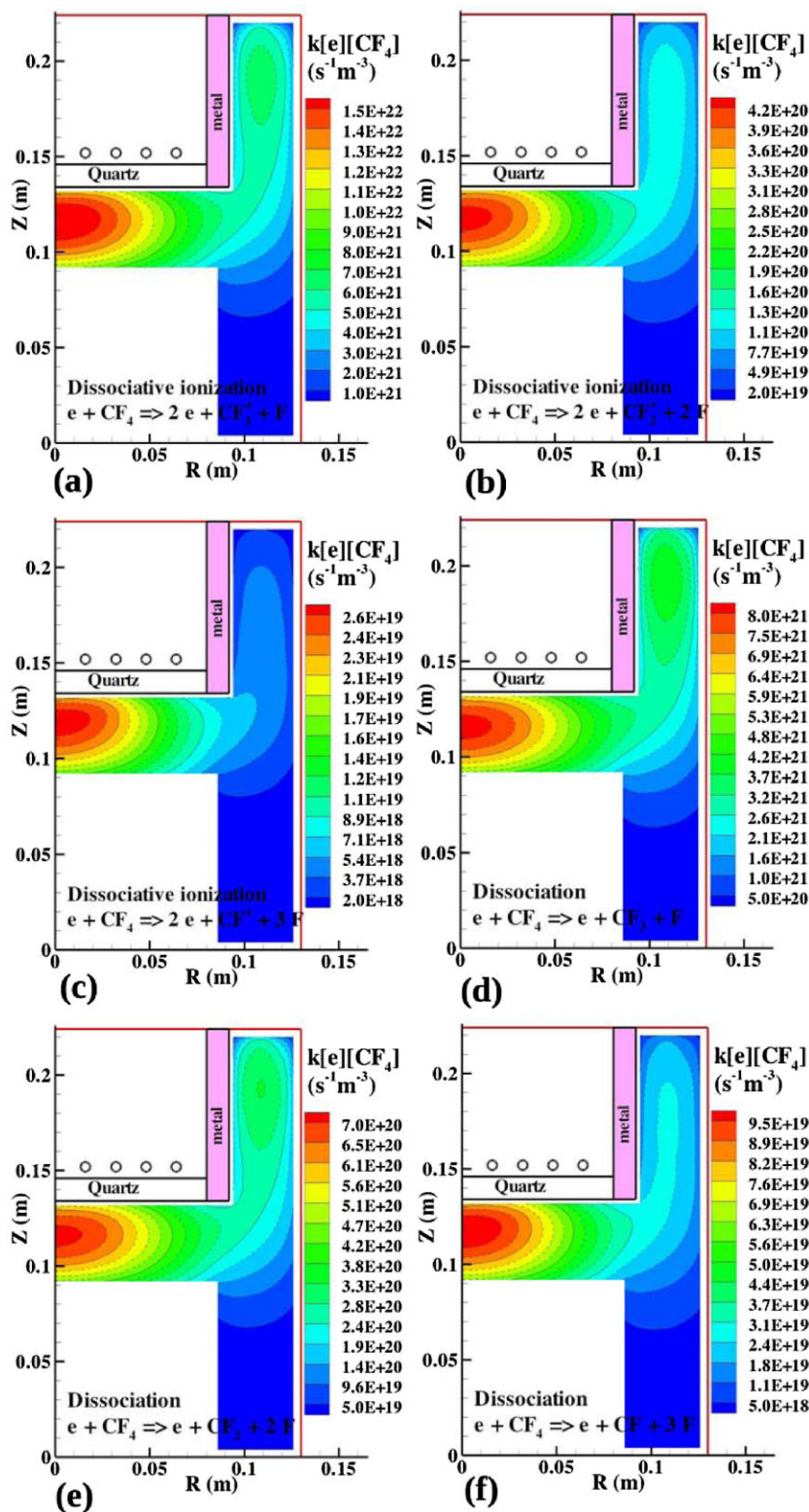


Figure 7. The two-dimensional contours of the production rate ($\text{m}^{-3} \text{s}^{-1}$) of a) dissociative ionization $e + \text{CF}_4 \rightarrow \text{CF}_3^+ + \text{F} + 2e$ (Fo5), b) dissociative ionization $e + \text{CF}_4 \rightarrow \text{CF}_2^+ + 2\text{F} + 2e$ (Fo6), c) dissociative ionization $e + \text{CF}_4 \rightarrow \text{CF}^+ + 3\text{F} + 2e$ (Fo7), d) dissociation $e + \text{CF}_4 \rightarrow \text{CF}_3 + \text{F} + e$ (F11), e) dissociation $e + \text{CF}_4 \rightarrow \text{CF}_2 + 2\text{F} + e$ (F12), and f) dissociation $e + \text{CF}_4 \rightarrow \text{CF} + 3\text{F} + e$ (F13).

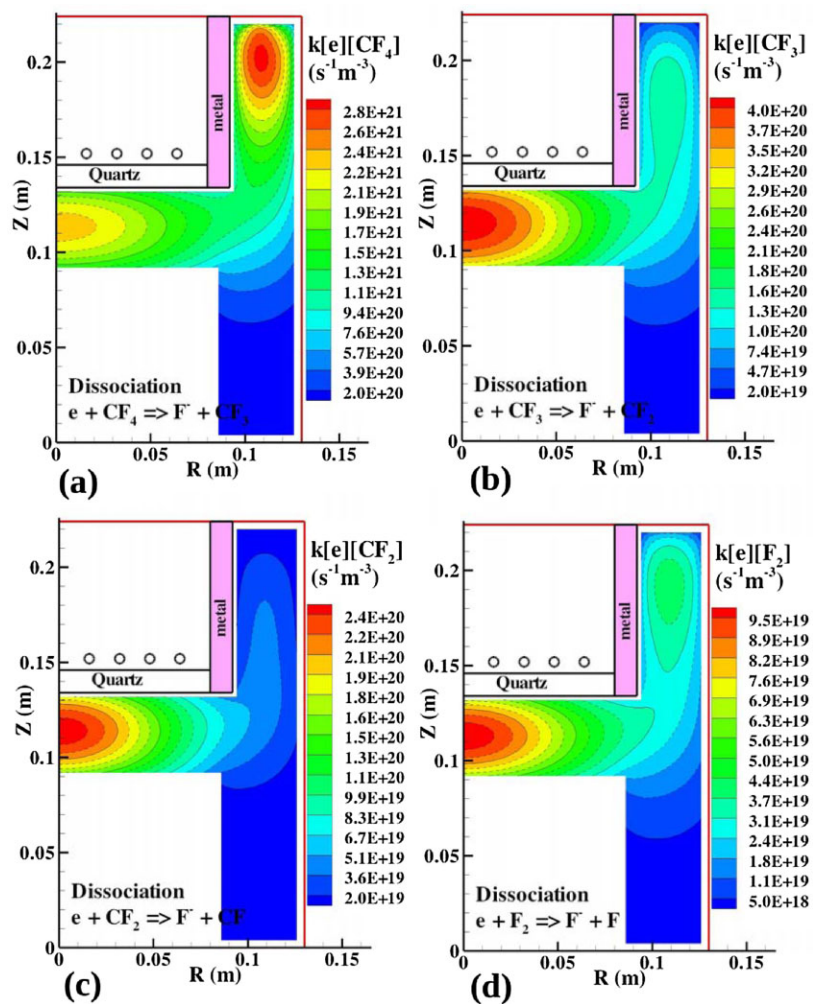


Figure 8. The two-dimensional contours of the production rate ($\text{m}^{-3}\text{s}^{-1}$) of a) dissociative attachment $e + \text{CF}_4 \rightarrow \text{CF}_3 + \text{F}^-$ (FNo1), b) dissociative attachment $e + \text{CF}_3 \rightarrow \text{CF}_2 + \text{F}^-$ (FNo2), c) dissociative attachment $e + \text{CF}_2 \rightarrow \text{CF} + \text{F}^-$ (FNo3) and d) dissociative attachment $e + \text{F}_2 \rightarrow \text{F} + \text{F}^-$ (FNo4).

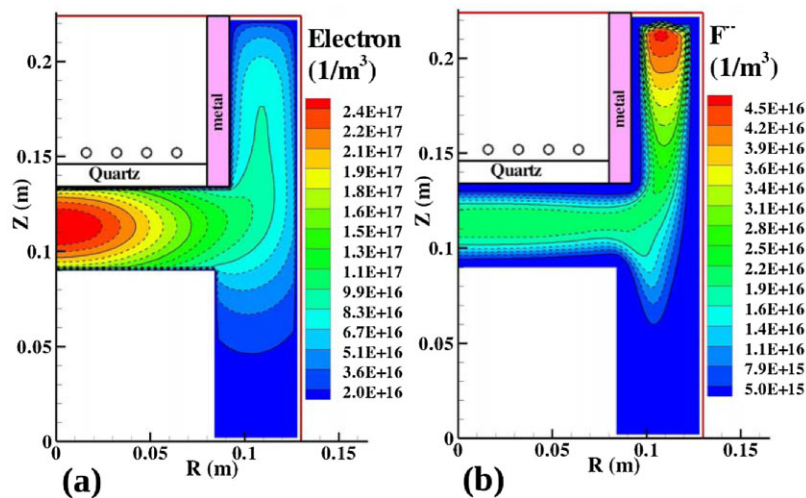


Figure 9. The two-dimensional contours of the concentration of a) electron and b) F^- .

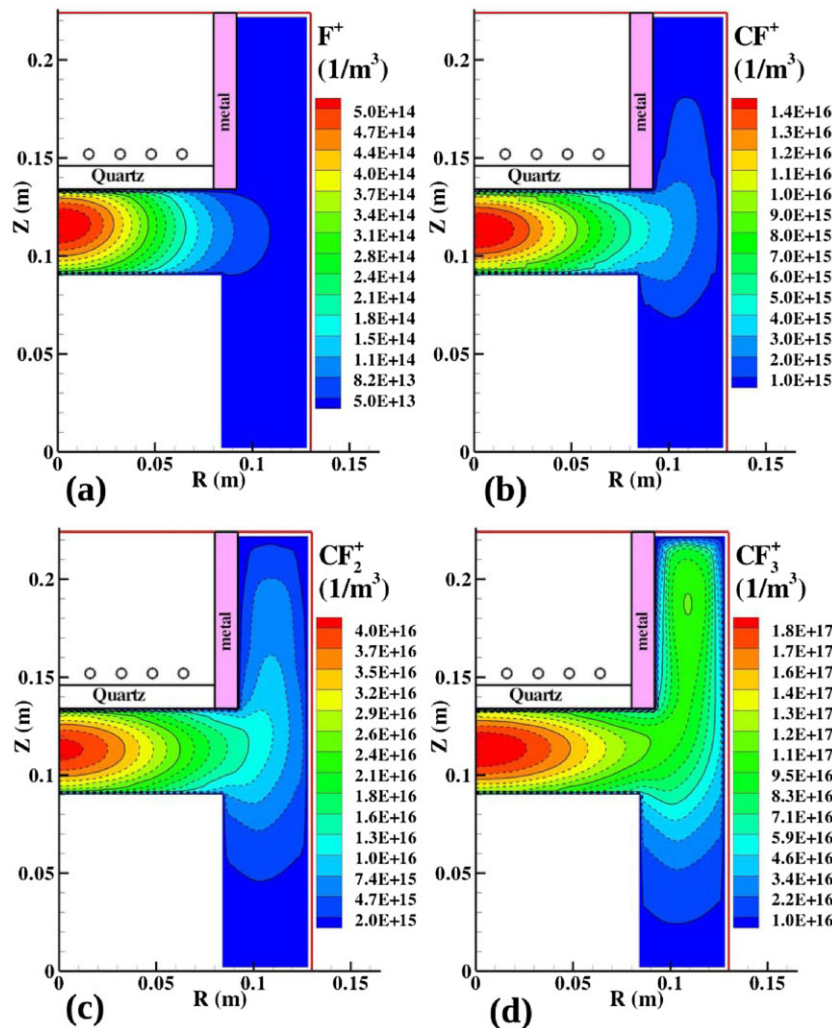


Figure 10. The two-dimensional contours of the concentration of a) F⁺, b) CF⁺, c) CF₂⁺, and d) CF₃⁺.

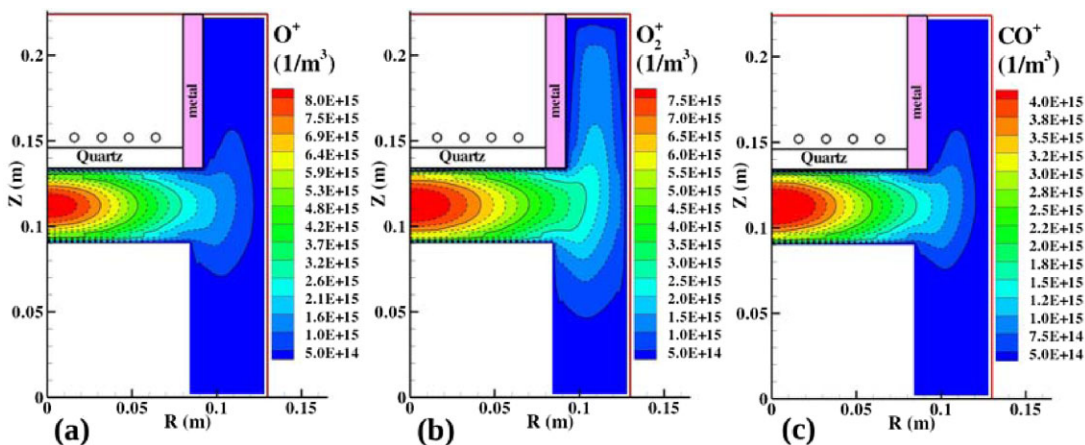


Figure 11. The two-dimensional contours of the concentration of a) O⁺, b) O₂⁺, and c) CO⁺.

which is similar to those observed by some experiments.^[30,41] In addition, the CF₃⁺ concentration not only peaks in the central core region but also in the region near gas inlet because of its low threshold energy of dissociative ionization (14.8 eV).

Figure 11 shows the spatial distributions of the concentrations of oxygen-containing positive charged species, including O⁺, O₂⁺, and CO⁺. In addition, Figure 12 presents the spatial distributions of the concentrations of silicon-containing positive charged species, including SiF⁺, SiF₂⁺, and SiF₃⁺ that are produced from volatile oxygen-containing and silicon-containing neutral species released during the etching process. O⁺ and O₂⁺ are generated by the ionization of their mother gases O and O₂ (Ox01, Ox04, Ox20, and Ox21 in Table 4). CO⁺ is the product of ionization of CO by the electron impact (Ox28 in Table 4). SiF_x⁺ (x=1–3) are generated by the dissociative ionization from their mother gases SiF_x (x=1–4) (SF01~SF06 in Table 5), and they are trapped in the central region by the electric field of ambipolar diffusion. It is noted that the concentration of SiF₃⁺ is about 10 times higher than those of SiF⁺ and SiF₂⁺ since the ionization threshold energy of SiF₃⁺ is lower than those of SiF⁺ and SiF₂⁺.

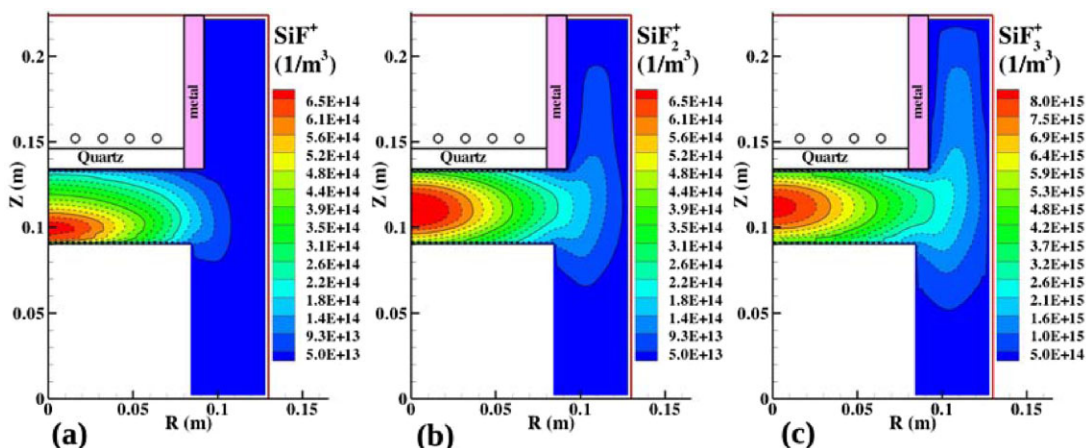


Figure 12. The two-dimensional contours of the concentration of a) SiF^+ , b) SiF_2^+ , and c) SiF_3^+ .

6.3.5. Spatial Distribution of Number Densities of Neutral and Radical Species

Figure 13 shows the spatial distribution of the concentrations of F and CF_x ($x = 1-3$), which are the most dominant species in etching the SiO_2 layer on the substrate. The results show that their concentrations are generally very high and only lower than the feedstock gas CF_4 . The results also show that, except the CF_3 that peaks both at the central core and inlet regions, all species are concentrated in the central core region. The concentration increases in the order of CF, CF_2 , and CF_3 mainly because of decreasing threshold energy of dissociation from CF_4 by the electron impact (F11~F13 in Table 2). In addition, the concentration of the neutral atom F is about seven times higher than that of CF_3 in the central core region due to the accumulated effect in this region through the above-mentioned various dissociation channels by the energetic electrons.

On the SiO_2 layers, including the substrate or the dielectric windows, the etching reactions are considered with the reactive radicals CF_x ($x = 0-3$) and the reactive ions. The etching products like O, O_2 , COF, COF_2 , and CO are produced at the surface and released into the plasma. These etching products (O, O_2 , COF, COF_2 , and CO) further change the gas-phase chemistry mostly due to the electron impact, especially near the SiO_2 layers.

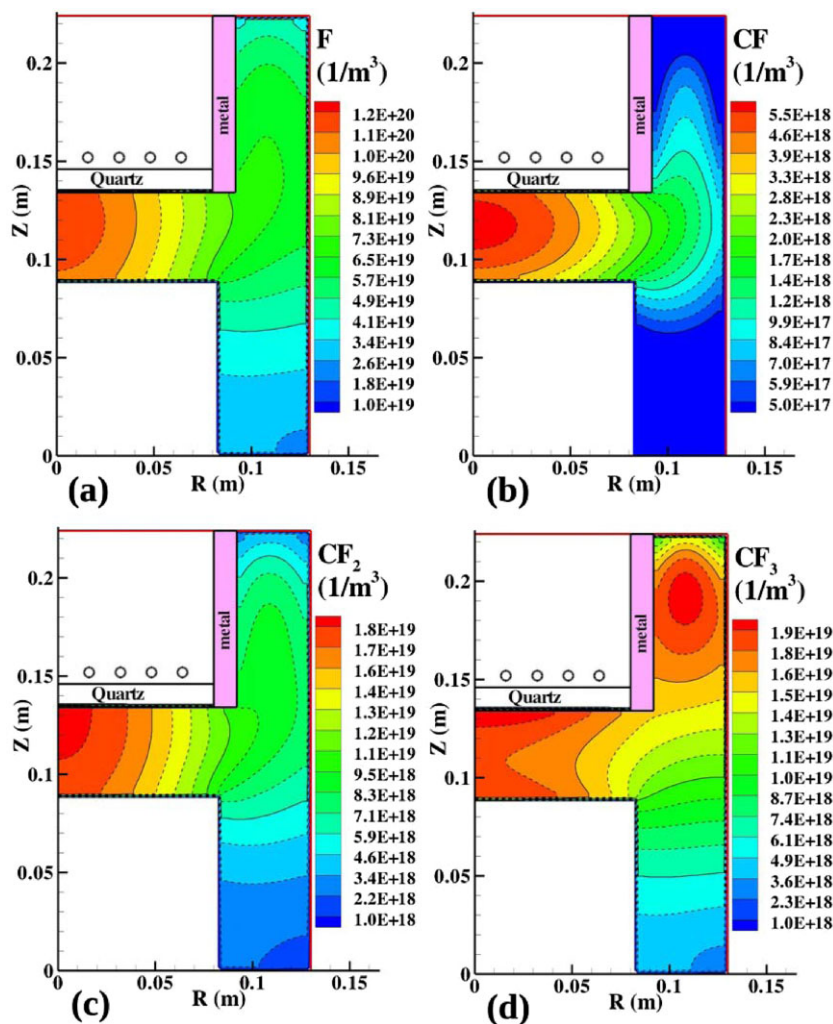


Figure 13. The two-dimensional contours of the concentration of a) F, b) CF, c) CF_2 , and d) CF_3 .

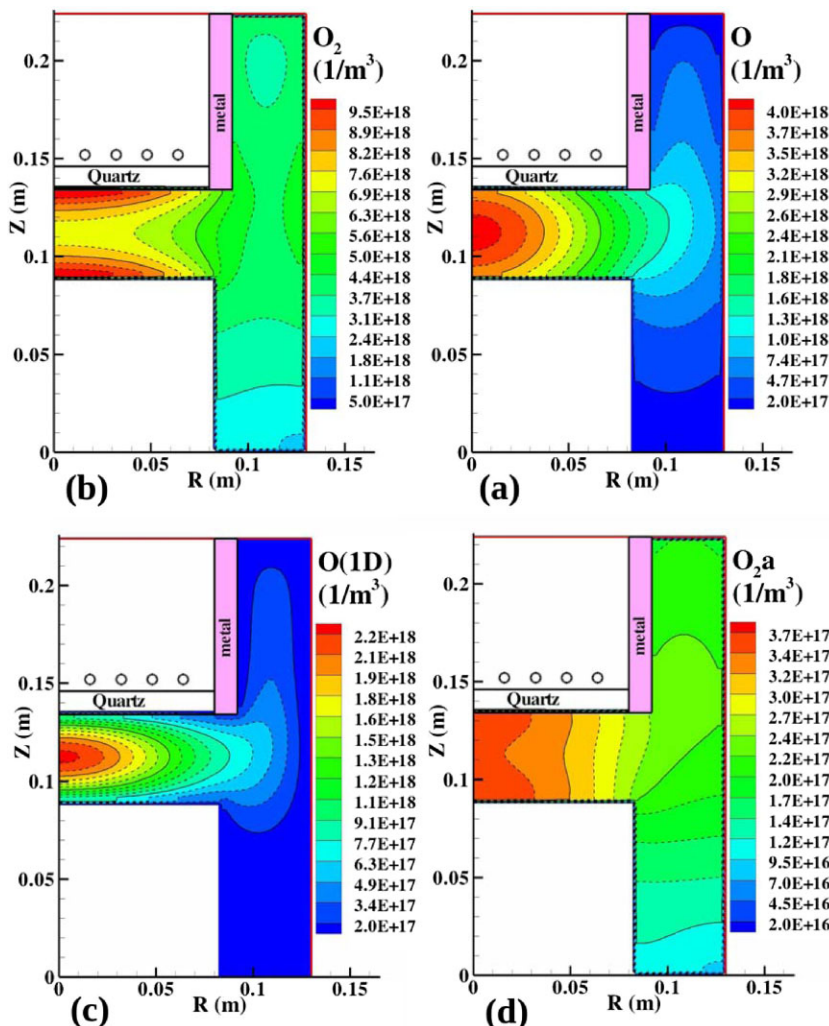
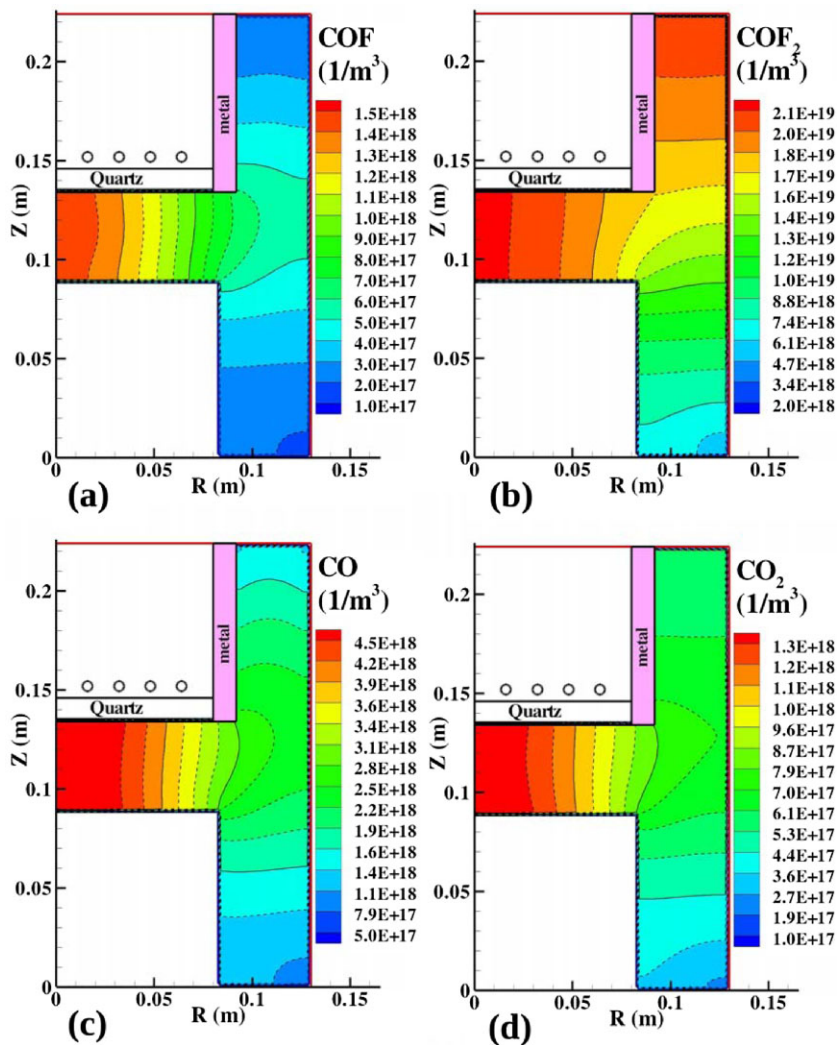


Figure 14. The two-dimensional contours of the concentration of a) O₂, b) O, c) O(1D), and d) O₂(a¹Δ_g).

Figure 14 shows the spatial distributions of several etching products related radical species. Figure 14a shows the distribution of the concentration of O₂ that is mainly produced through the ion-enhanced chemical etching and the ion-enhanced chemical sputtering by F (S3 and S4, respectively, in Table 6) at the SiO₂ layers on the quartz window and substrate. The maximal values are found at the dielectric surfaces and decreases towards at the central core region where the electrons are most energetic that dissociate and excite the oxygen efficiently which forms O and O(1D), and O₂(a) (Ox02, Ox10, Ox16, and Ox17 in Table 4). The corresponding distributions are shown in Figure 14b–d, respectively. Because of this, the concentrations of O and O(1D), and O₂(a) become very high at the core region, especially a high amount of O is produced due to a high degree of the dissociation of O₂ caused by the electron impact. Even though O is released from the

surface due to physical sputtering (S1), it can also recombine with each other into O₂ on substrate surface (W15).

Figure 15 presents the spatial distributions of the number densities of carbonous oxide related products such as COF, COF₂, CO, and CO₂. COF. These species are produced through O generated from the surface reactions with the fluorocarbon radicals, but are lost by the collision with some of the abundant radicals such as CF_x. Although COF₂ can be generated on the substrate by the etching process (S8 in Table 6), they are mostly produced by the reaction of CF₃ and O in the central core region and near the gas inlet region where the concentrations of either/both CF₃ and O are high. CO and CO₂ are mainly generated in the core region by the gas-phase reactions between COF_x and CF_x (Ox31, Ox32, Ox34, Ox36, Ox38, and Ox39 in Table 4) or the surface reactions (S7 in Table 6).



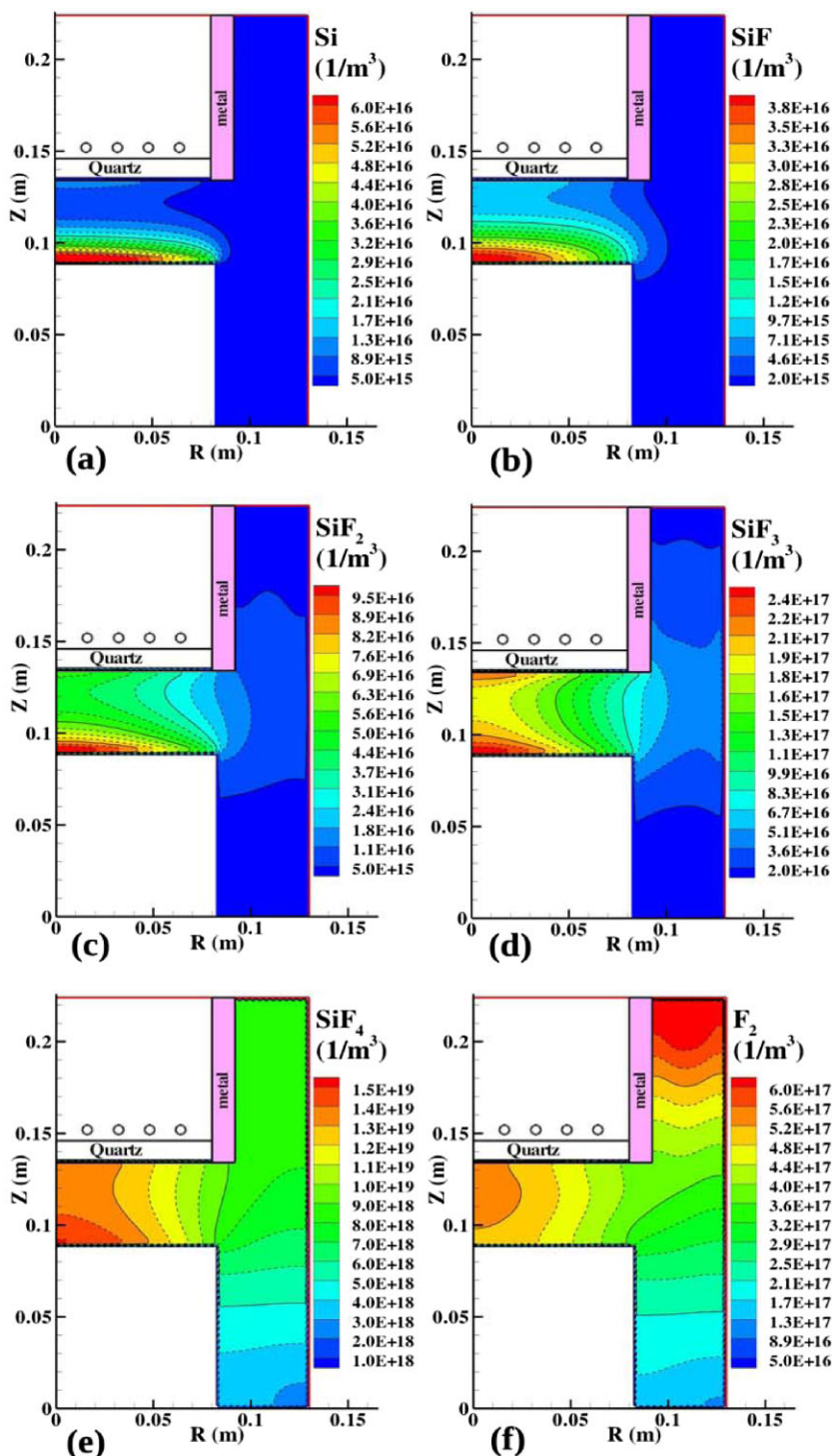
■ Figure 15. The two-dimensional contours of the concentration of a) COF, b) COF₂, c) CO and d) CO₂.

Figure 16a–e illustrates the spatial distributions of the concentrations of SiF_x (x = 0–4) which show that most of them are concentrated near the substrate region since these species are released through the etching processes by the bombarding ions and radicals on the SiO₂ layer of the substrate. In addition, more SiF_x (x = 0–4) are also produced from the SiO₂ dielectric window as x increases. Simulation shows that SiF₄ is the most dominant etching products, which was also consistently observed in many experiments.^[23,28,67] It is noted that the volatile SiF_x (x = 0–3) strongly depends on the surface coverage of CF_x (θ_{CF_x}), the volatile SiF₄ strongly depends on the surface coverage of F (θ_F). It is obvious that when θ_F is the dominant coverage on either substrate or dielectric windows, θ_{CF_x} only covers on the substrate since ion bombarding energy is lower on the dielectric window. The distribution of F₂ as shown in Figure 16f demonstrates that the highest concentration

occurs near the gas inlet, since F₂ is mainly produced from the de-attachment recombination of F⁻ and F (FN11 in Table 3) which are both rich near the gas inlet

6.3.6. Spatially Averaged Number Densities of Chemical Species

The concentrations of the charged and neutral species averaged spatially over the core region of the reactor are presented in Figures 17 and 18, respectively. It is obvious that the positive ion CF₃⁺ is the most dominant charged species with a concentration of ~10¹⁷ m⁻³, that is only exceeded by the electrons. The simulated trend of the concentration is CF₃⁺ > CF₂⁺ > CF⁺, which is consistent with that observed in the experiments.^[30,31,66] The negative ion F⁻ is also found to be abundant with a concentration of ~10¹⁶ m⁻³. The value is smaller than that (~10¹⁷ m⁻³)



■ Figure 16. The two-dimensional contours of the concentration of a) Si, b) SiF, c) SiF₂, d) SiF₃, e) SiF₄, and f) F₂.

estimated by Rao et al.^[30] through a simple chemical kinetic model with the use of some experimental data; however, its validity needs to be confirmed. In addition, except the CF₄ which is the feedstock gas, F is the most dominant radical species with a concentration of $\sim 10^{20} \text{ m}^{-3}$ that explains

why the coverage of fluorine on the substrate is the largest among all species. The simulated number density of CF_x is found to increase weakly as a function of increasing x ($x = 1-3$), as had also been observed in the APMS measurements^[41] and the FTIR measurements.^[32] The COF₂

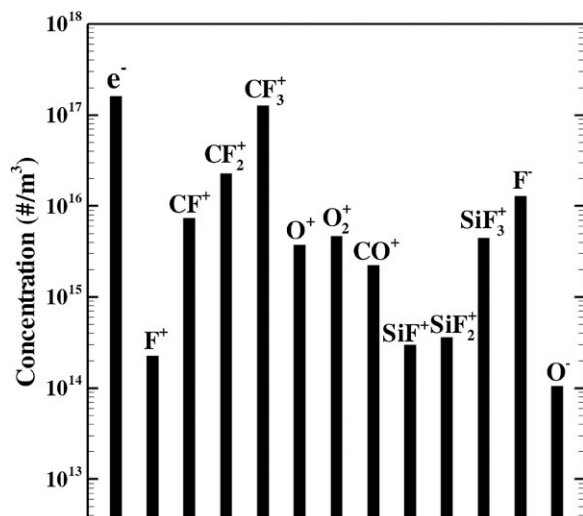


Figure 17. The concentrations of the charged species averaged spatially over the core region of an ICP-GECC reactor.

concentration is approximately equal to the concentration of SiF_4 , which was also observed in several typical FTIR measurements.^[28,29]

6.3.7. Surface Coverage

Figure 19 shows several radial distributions of the surface coverage on the substrate. The atomic fluorine surface coverage is found to be the most dominant one in our simulation since the atomic fluorine fluxes are much larger than the fluorocarbon radical fluxes (shown in Figure 20), which results in a net etching process on the substrate surface.^[68] The resulting ratio among various kinds of coverage, $\theta_F:\theta_P$ (deposition):uncovered ($1 - \theta_F - \theta_{CF_x} - \theta_P$,

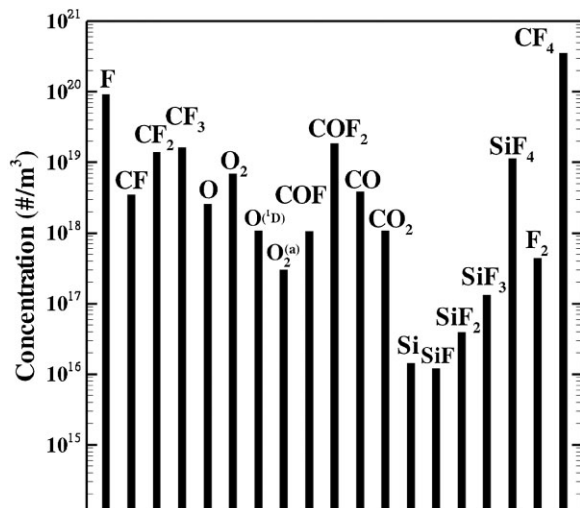


Figure 18. The concentrations of the neutral species averaged spatially over the core region of an ICP-GECC reactor.

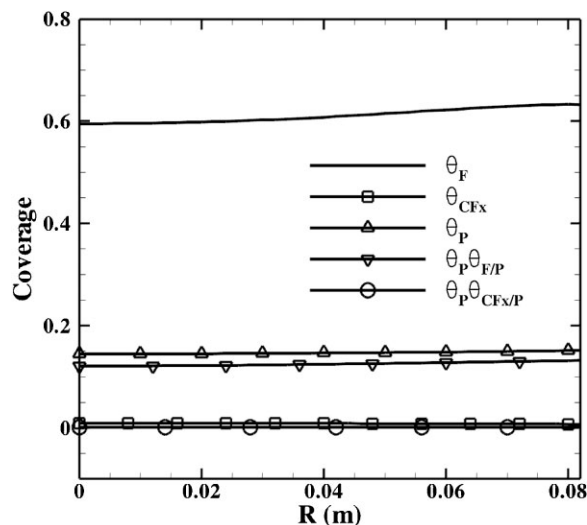


Figure 19. The various kinds of surface coverage as a function of the radial distance on the substrate.

physical sputtering), is approximately 0.6:0.15:0.2. It is obvious that the etching process is mainly controlled by the fluorine surface coverage, which makes the most of the etching products generated from the fluorine surface coverage.

6.3.8. Spatial Distribution of Etching Rate and Particle Fluxes on the Substrate

Figure 20 presents the radial distributions of fluxes of the ions CF_x^+ ($x = 1-3$) and the radicals F and CF_x ($x = 1-3$), and the etching rate on the substrate. All fluxes decrease

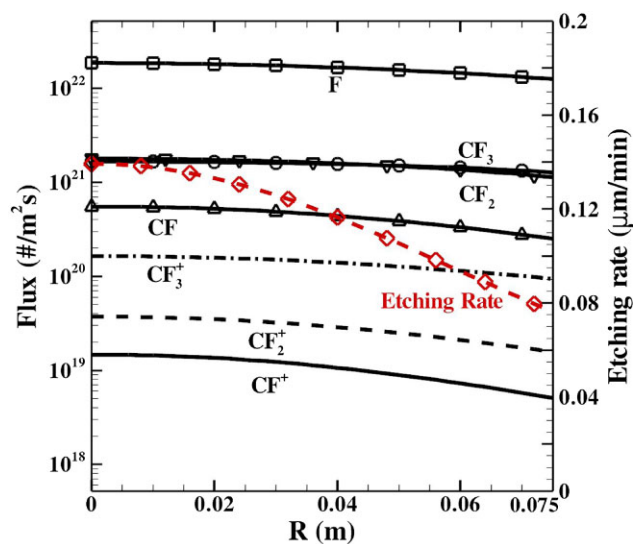


Figure 20. The radial distributions of fluxes of the ions CF_x^+ ($x = 1-3$) and the radicals F and CF_x ($x = 1-3$), and the etching rate on the substrate.

monotonically towards the edge of substrate as expected due to decreasing power absorption and lower static electric field. Near the central region of the substrate, the fraction of CF₃⁺, CF₂⁺, and CF⁺ fluxes is approximately 70, 20, and 10%, respectively, while the fraction of F, the total CF_x (x = 1–3) and total CF_x⁺ (x = 1–3) fluxes is roughly 90, 9, and 1%, respectively, in a global sense. In other words, the ratio of the atomic fluorine flux to the total ion flux is ~100, and the ratio of the total fluorocarbon radical flux to the total ion flux is ~10. Therefore, the etching process is always the dominant surface reactions compared to the other processes such as deposition or sputtering. In addition, the current predicted etch rate that decreases from the central to the edge is roughly 100 nm min⁻¹ on the average which is reasonable compared to those found in the experiments.^[32,69]

7. Conclusion

A parallel two-dimensional axisymmetric fluid model coupled with the Maxwell's equation and surface site balance model has been developed to study the complex CF₄ plasma physics and chemistry in a GECRC-ICP chamber in this paper. Super-linear speedup can be obtained up to 26 processors for a grid size of 122 × 179 cells considering 32 species, 96 gas reactions and 27 surface reactions by a combination of Block-Jacobi and GMRES, respectively, as the preconditioner and linear matrix solver. We have verified the parallel code by the good agreement with previous simulations under the same test conditions. The numerical results of the GECRC-ICP simulations indicate that CF₃⁺ is the dominant charged species while F⁻ is comparable to the concentration of electron. The most abundant reactive radical species is found to be F. The etching products, such as SiF_x and O₂ from the substrate, are found to be appreciable in the order of 10% compared to the feedstock CF₄ near the substrate. In addition, the predicted trend of the magnitude of species concentration, such as CF₃⁺ > CF₂⁺ > CF⁺ and CF₃ > CF₂ > CF, is consistent with the experimental observations. Because the F flux is much larger than those of the CF_x and the ions, the F coverage becomes the most dominant one on the substrate. With the developed tool, an optimized etching rate and reactive fluxes on substrate surface can be predicted for a better design of an ICP chamber.

Acknowledgements: The 1st and the corresponding author have received Lam Research Award 2012 in Taiwan because of this research work. The authors would also like to express their sincere gratitude to the financial support of National Science Council of Taiwan through the grant NSC-101-2221-E-009-041-MY3.

Received: September 29, 2013; Revised: January 12, 2014;
Accepted: January 14, 2014; DOI: 10.1002/ppap.201300134

Keywords: CF₄ discharge; fluid model; inductively coupled plasma (ICP); parallel computing; surface model

- [1] T. Desmet, R. Morent, N. D. Geyter, C. Leys, E. Schacht, P. Dubruel, *Biomacromolecules* **2009**, *10*, 2351.
- [2] E. Gogolides, P. Vauvert, G. Kokkoris, G. Turban, A. G. Boudouvis, *J. Appl. Phys.* **2000**, *88*, 5570.
- [3] G. Kokkoris, E. Gogolides, A. G. Boudouvis, *J. Appl. Phys.* **2002**, *91*, 2697.
- [4] S. M. George, *Chem. Rev.* **2010**, *110*, 111.
- [5] H. Kim, *J. Vacuum Sci. Technol. B Microelectron. Nanometer Struct.* **2003**, *21*, 2231.
- [6] G. Bugnon, A. Feltrin, F. Meillaud, J. Bailat, C. Ballif, *J. Appl. Phys.* **2009**, *105*, 064507.
- [7] B. Wu, A. Kumar, S. Pamarthy, *J. Appl. Phys.* **2010**, *108*, 051101.
- [8] R. J. Shul, S. J. Pearton, *Handbook of Advanced Plasma Processing Techniques*, 1st ed., Springer, Berlin, Heidelberg, Germany **2000**.
- [9] H. Treichel, G. Ruhl, P. Ansmann, R. Würzl, C. Müller, M. Dietlmeier, *Microelectron. Eng.* **1998**, *40*, 1.
- [10] I. Morey, A. Asthana, *Solid State Technol.* **1999**, *42*, 71.
- [11] H. C. Kim, F. Iza, S. S. Yang, M. Radmilović-Radjenović, J. K. Lee, *J. Phys. D Appl. Phys.* **2005**, *38*, R283.
- [12] S. Hamaguchi, *IBM J. Res. Dev.* **1999**, *43*, 199.
- [13] M. M. Turner, *J. Phys. D Appl. Phys.* **2009**, *42*, 194008.
- [14] T. Kimura, K. Ohe, *Plasma Sources Sci. Technol.* **1999**, *8*, 553.
- [15] T. Kimura, K. Ohe, *J. Appl. Phys.* **2002**, *92*, 1780.
- [16] T. Kimura, M. Noto, *J. Appl. Phys.* **2006**, *100*, 063303.
- [17] T. Kimura, K. Hanaki, *Jpn J. Appl. Phys.* **2008**, *47*, 8537.
- [18] D. B. Hash, D. Bose, M. V. V. S. Rao, B. A. Cruden, M. Meyyappan, S. P. Sharma, *J. Appl. Phys.* **2001**, *90*, 2148.
- [19] D. Bose, D. Hash, T. R. Govindan, M. Meyyappan, *J. Phys. D Appl. Phys.* **2001**, *34*, 2742.
- [20] M. W. Kiehlbauch, D. B. Graves, *J. Appl. Phys.* **2001**, *89*, 2047.
- [21] K. N. Ostrikov, I. B. Denysenko, E. L. Tsakadze, S. Xu, R. G. Storer, *J. Appl. Phys.* **2002**, *92*, 4935.
- [22] J. W. Coburn, H. F. Winters, *J. Vacuum Sci. Technol.* **1979**, *16*, 391.
- [23] J. W. Coburn, H. F. Winters, T. J. Chuang, *J. Appl. Phys.* **1977**, *48*, 3532.
- [24] C. J. Choi, O. S. Kwon, Y. S. Seol, Y. W. Kim, I. H. Choi, *J. Vacuum Sci. Technol. B Microelectron. Nanometer Struct.* **2000**, *18*, 811.
- [25] J. K. Olthoff, Y. Wang, *Papers from the 45th National Symposium of the American Vacuum Society*, **1999**, *17*, 1552.
- [26] G. A. Hebner, *J. Appl. Phys.* **2001**, *90*, 4938.
- [27] G. A. Hebner, *J. Appl. Phys.* **2001**, *89*, 900.
- [28] B. A. Cruden, M. V. V. S. Rao, S. P. Sharma, M. Meyyappan, *Plasma Sources Sci. Technol.* **2002**, *11*, 77.
- [29] B. A. Cruden, M. V. V. S. Rao, S. P. Sharma, M. Meyyappan, *J. Appl. Phys.* **2003**, *93*, 5053.
- [30] M. V. V. S. Rao, S. P. Sharma, M. Meyyappan, *Plasma Sources Sci. Technol.* **2002**, *11*, 397.
- [31] M. V. V. S. Rao, S. P. Sharma, B. A. Cruden, M. Meyyappan, *Plasma Sources Sci. Technol.* **2002**, *11*, 69.
- [32] B. Zhou, E. A. Joseph, L. J. Overzet, M. J. Goeckner, *J. Vacuum Sci. Technol. A Vacuum Surf. Films* **2006**, *24*, 114.
- [33] Y. Hikosaka, M. Nakamura, H. Sugai, *Jpn. J. Appl. Phys.* **1994**, *33*, 2157.
- [34] D. Zhang, M. J. Kushner, *J. Appl. Phys.* **2000**, *87*, 1060.
- [35] H. Fukumoto, I. Fujikake, Y. Takao, K. Eriguchi, K. Ono, *Plasma Sources Sci. Technol.* **2009**, *18*, 045027.
- [36] E. W. McDaniel, E. A. Mason, *The Mobility and Diffusion of Ions in Gases*, 99th ed., John-Wiley & Sons, Hoboken, New Jersey, USA **1973**.

- [37] C.-C. Hsu, M. A. Nierode, J. W. Coburn, D. B. Graves, *J. Phys. D Appl. Phys.* **2006**, *39*, 3272.
- [38] B. Ramamurthi, D. J. Economou, *J. Vacuum Sci. Technol. A Vacuum Surf. Films* **2002**, *20*, 467.
- [39] M. A. Lieberman, A. J. Lichtenberg, *Principles of Plasma Discharges and Materials Processing*, 2nd ed., Wiley-Interscience, **2005**.
- [40] P. Ho, J. E. Johannes, R. J. Buss, E. Meeks, *J. Vacuum Sci. Technol. A Vacuum Surf. Films* **2001**, *19*, 2344.
- [41] H. Singh, J. W. Coburn, D. B. Graves, *J. Vacuum Sci. Technol. A Vacuum Surf. Films* **2001**, *19*, 718.
- [42] L. G. Christophorou, J. K. Olthoff, M. V. V. S. Rao, *J. Phys. Chem. Ref. Data* **1996**, *25*, 1341.
- [43] M. A. Lennon, K. L. Bell, H. B. Gilbody, J. G. Hughes, A. E. Kingston, M. J. Murray, F. J. Smith, *J. Phys. Chem. Ref. Data* **1988**, *17*, 1285.
- [44] V. Tarnovsky, P. Kurunczi, D. Rogozhnikov, K. Becker, *Int. J. Mass Spectrometry Ion Processes* **1993**, *128*, 181.
- [45] R. E. Center, A. Mandl, *J. Chem. Phys.* **1972**, *57*, 4104.
- [46] W. L. Morgan, *Plasma Chem. Plasma Process* **1992**, *12*, 449.
- [47] Y. Itikawa, A. Ichimura, *J. Phys. Chem. Ref. Data* **1990**, *19*, 637.
- [48] Y. Itikawa, *J. Phys. Chem. Ref. Data* **2009**, *38*, 1.
- [49] Y. Itikawa, A. Ichimura, K. Onda, K. Sakimoto, K. Takayanagi, Y. Hatano, M. Hayashi, H. Nishimura, S. Tsurubuchi, *J. Phys. Chem. Ref. Data* **1989**, *18*, 23.
- [50] Y. Itikawa, *J. Phys. Chem. Ref. Data* **2002**, *31*, 749.
- [51] B. Eliasson, *Basic Data for Modelling of Electrical Discharges in Gases: Oxygen*, ABB Asea Brown Boveri, Zürich, Switzerland **1986**.
- [52] D. Rapp, P. Englander-Golden, *J. Chem. Phys.* **1965**, *43*, 1464.
- [53] R. Basner, M. Schmidt, E. Denisov, K. Becker, H. Deutsch, *J. Chem. Phys.* **2001**, *114*, 1170.
- [54] T. Nakano, H. Sugai, *J. Phys. D Appl. Phys.* **26**, **1993**, 1909.
- [55] I. Iga, M. V. V. S. Rao, S. K. Srivastava, J. C. Nogueira, *Z. Phys. D Atoms Molecules Clusters* **1992**, *24*, 111.
- [56] T. R. Hayes, R. J. Shul, F. A. Baiocchi, R. C. Wetzel, R. S. Freund, *J. Chem. Phys.* **1988**, *89*, 4035.
- [57] R. J. Shul, T. R. Hayes, R. C. Wetzel, F. A. Baiocchi, R. S. Freund, *J. Chem. Phys.* **1988**, *89*, 4042.
- [58] T. R. Hayes, R. C. Wetzel, F. A. Baiocchi, R. S. Freund, *J. Chem. Phys.* **1988**, *88*, 823.
- [59] G. Hagelaar, L. Pitchford, *Plasma Sources Sci. Technol.* **2005**, *14*, 722.
- [60] National Institute of Standards and Technology, <http://kinetics.nist.gov/kinetics/>
- [61] National Institute for Fusion Science DATABASE, <http://www.nifs.ac.jp/>
- [62] D. P. Lymberopoulos, V. I. Kolobov, D. J. Economou, *J. Vacuum Sci. Technol. A Vacuum Surf. Films* **1998**, *16*, 564.
- [63] Y. Saad, *Iterative Methods for Sparse Linear Systems*, 2nd ed., Society for Industrial and Applied Mathematics, Philadelphia, Pennsylvania, USA **2003**.
- [64] S. Balay, J. Brown, K. Buschelman, W. D. Gropp, D. Kaushik, M. G. Knepley, L. C. McInnes, B. F. Smith, H. Zhang, PETSc Web Page, **2012**.
- [65] MPICH | High-performance and Portable MPI, <http://www.mpich.org/>
- [66] H. Fukumoto, K. Ono, K. Takahashi, Plasma Chemical Behavior of Inductively Coupled Fluorocarbon Plasmas, *17th International Symposium on Plasma Chemistry*, Toronto, Ontario, Canada **2005**.
- [67] B. A. Cruden, M. V. V. S. Rao, S. P. Sharma, M. Meyyappan, *J. Appl. Phys.* **2002**, *91*, 8955.
- [68] H. Tanaka, T. Ishikawa, T. Masai, T. Sagara, L. Boesten, M. Takekawa, Y. Itikawa, M. Kimura, *Phys. Rev. A* **1998**, *57*, 1798.
- [69] F. H. Bell, O. Joubert, G. S. Oehrlein, Y. Zhang, D. Vender, *J. Vacuum Sci. Technol. A Vacuum Surf. Films* **1994**, *12*, 3095.
- [70] W. M. Haynes, *CRC Handbook of Chemistry and Physics*, 92nd edition (Hardback), CRC Press, Boca Raton, Florida, USA.
- [71] J.-P. Bouanich, *J. Quant. Spectrosc. Radiat. Transf.* **1992**, *47*, 243.